Remote Sensing of Environment 198 (2017) 213–228

Contents lists available at ScienceDirect

Remote Sensing of Environment

journal homepage: www.elsevier.com/locate/rse

Retrieval of Secchi disk depth from a reservoir using a semi-analytical scheme

Thanan Rodrigues [a], Enner Alcântara [b,*], Fernanda Watanabe [a], Nilton Imai [a]

[a] São Paulo State University (Unesp), Department of Cartography, 305 Roberto Simonsen Street, Presidente Prudente 19060-900, SP, Brazil
[b] São Paulo State University (Unesp), Department of Environmental Engineering, Rodovia Presidente Dutra, Km 137.8, São José dos Campos 12247-004, SP, Brazil

ARTICLE INFO

Article history:
Received 6 November 2016
Received in revised form 6 June 2017
Accepted 9 June 2017
Available online 6 July 2017

Keywords:
Optical properties
Inland waters
Tropical reservoirs
Water clarity

ABSTRACT

The mechanistic model reported in Lee et al. (2015) estimating the Secchi disk depth (Z_{SD}) was applied to an oligo- to mesotrophic reservoir in Brazil. The model was originally validated with data covering lake, oceanic, and coastal waters; however, the model used the quasi-analytical algorithm (QAA) designed for optically deep waters as input and was applied to oceanic and coastal waters to derive absorption [a] and backscattering [b_b] coefficients. The hypothesis is that the use of QAA_{v5} (http://www.ioccg.org/groups/Software_OCA/QAA_v5.pdf) to estimate both a and b_b (step M1) to retrieve K_d (step M2) and Z_{SD} (step M3) will lead to errors caused by M1 preventing an accurate estimate in oligo- to mesotrophic water. To test this hypothesis, data collected in three field trips were used to apply the mechanistic model based on the spectral bands from OLI/Landsat-8, (often applied to oceanic and coastal waters), and multispectral instrument (MSI)/Sentinel-2 bands (applied to QAA designed for very turbid inland water). The impact of step M1 over steps M2 and M3 was analyzed by the error analysis. The mean absolute percentage error (MAPE) for K_d using QAA_{v5} ranged between 10.35% and 19.76%, while the error using QAA_{M14} varied between 12.68% and 28.29%. Regarding the errors of step M3 and applying QAA_{v5}, the total root-mean-square difference (RMSD) varied from 0.55 to 1.18 m and MAPE ranged between 12.86% and 31.17%, while the RMSD ranged between 0.70 and 1.50 m and MAPE varied from 14.33% to 39.13% when using QAA_{M14}. However, the result from QAA_{v5} showed a better correlation with *in situ* data, although underestimating K_d and Z_{SD}. Therefore, a modified version of QAA_{v5} (QAA_{R17}) was evaluated. The results showed an improvement of K_d (MAPE ranging between 8.89% to 18.76%) and Z_{SD} (RMSD ranging between 0.32 and 0.90 m and MAPE ranging between 8.65 and 19.75%), bringing the values close to the 1:1 line. The largest error was observed for the data of the second field trip, where the bio-optical properties showed a horizontal gradient along the reservoir. In addition, the magnitude of the remote sensing reflectance (R_{rs}) also varied depending on the water quality. Thus, with respect to Z_{SD} mapping, this research showed that environments with a high variability in R_{rs} can limit the accurate estimation of inherent optical properties (IOPs) based on QAA_{v5}. Therefore, the limiting step of the model was attributed to M1, which means that the mechanistic model from Lee et al. (2015) can be considered an universal approach if M1 is modified based on the type of water.

1. Introduction

The water clarity can be considered to be key information for the evaluation of the water quality. The attenuation of light with depth is dictated by water molecules, phytoplankton productivity, and particle and dissolved matter distribution (Kirk, 1975; Mobley, 1994). The interaction of solar radiation and in-water constituents can impact the photosynthesis and photo-oxidation (Doron et al., 2007). The attenuation of light can be described by the vertical diffuse attenuation coefficient, K_d (m^{-1}), and the beam attenuation coefficient, c (m^{-1}). The inverse of c is related to the horizontal visibility (Zaneveld and Pegau, 2003), while the vertical visibility, analogous to the Secchi disk depth (Z_{SD}), is the inverse of the sum of $K_d + c$ (Tyler, 1968; Preisendorfer, 1986). The Z_{SD} is a measure of transparency in the vertical direction and the trophic state of a waterbody; thus, much effort has been made to estimate Z_{SD} of oceanic, coastal, and inland water (Buiteveld, 1995; Doron et al., 2007; Majozi et al., 2014; Fukushima et al., 2015; Lee et al., 2015).

The relationship between Z_{SD} and K_d is not universal; the correlation between Z_{SD} and K_d is almost the same as that between Z_{SD} and c (Aas et al., 2014; Lee et al., 2015). Therefore, empirical and semi-analytical approaches were carried out to derive K_d and Z_{SD}. Mueller (2000a) empirically derived $K_d(490)$ of seawater based on the band ratio of water-leaving radiances at 490 and 555 nm. Morel (1988) proposed an empirical relationship between $K_d(\lambda)$ and the chlorophyll concentration for oceanic water, which was further updated by Morel and

* Corresponding author.
E-mail address: enner.alcantara@ict.unesp.br (E. Alcântara).

http://dx.doi.org/10.1016/j.rse.2017.06.018
0034-4257/

Maritorena (2001). Based on the radiative transfer theory, Lee et al. (2005a) proposed a semi-analytical model aiming to retrieve the K_d of ocean water (Gordon et al., 1975).

All previously presented models are focused on seawater properties; therefore, the optical water quality is different from that of inland water with high absorption coefficients. Buiteveld (1995) introduced a semi-analytical way to model Z_{SD} and diffuse attenuation of photosynthetically active radiation (PAR), $K_d(PAR)$, using data from four eutrophic lakes in the Netherlands. The model is based on the relationship described in Tyler (1968) and Preisendorfer (1986). Recently, good results were achieved with the empirical Z_{SD}-based model for inland water. Majozi et al. (2014) retrieved $K_d(490)$ to estimate the euphotic depth (Z_{eu}) in Lake Naivasha, Kenya, and found that the ratio between the bands at 560 and 490 nm yielded the best outcome for Z_{eu}. Al Kaabi et al. (2016) tested several approaches to derive $K_d(490)$ and then correlated it to the *in situ* Z_{SD}; they found a reasonable relationship ($R^2 = 0.62$, total root-mean-square difference, RMSD = 26.68%) between $K_d(490)$ and Z_{SD} calculated using the model reported in Lee et al. (2005a).

The semi-analytical model from Lee et al. (2015) based on radiative transfer was reformulated to derive Z_{SD} relying only on K_d at a wavelength representing the maximum transparency. This new model was validated using a large dataset covering different optical environments such as oceanic, coastal, and inland water. The average absolute error, abe, was ~18% and R^2 was 0.96 between measured and estimated Z_{SD} (Lee et al., 2016). The inherent optical properties (IOPs) predicted using the quasi-analytical algorithm (QAA) were used as input, considering the reference wavelength (λ_0) at 55 × or 670 nm (Lee et al., 2016). The native QAA was more applicable to water with lower absorption coefficients; however, many reparameterizations were conducted aiming to use the algorithm for inland water (Lee et al., 2002, 2009; Yang et al., 2013; Mishra et al., 2014; Watanabe et al., 2016a).

Several authors highlighted important liminations of the native QAA for applications to inland water, which might affect its accuracy (Le et al., 2009; Yang et al., 2013), such as the estimation of the total absorption coefficient at a reference wavelength, $a(\lambda_0)$, which was based on synthetic data. Secondly, the spectral power of the particle backscattering coefficient, η, was calibrated considering the data from open oceans or coastal water. The last issue concerns the use of synthetic data for the estimation of the phytoplankton absorption. Those steps were listed by Lee et al. (2002) as second order of importance because they have a narrow range of variation and small influence on the output; however, the authors mentioned that they affect the final product and therefore improvements must be carried out considering regional and seasonal information or using better algorithms (Lee et al., 2010).

The Z_{SD} model uses the remote sensing reflectance (R_{rs}) to estimate the IOPs and then K_d, which is used to estimate Z_{SD}. The literature showed that the QAA_{v5} fails in estimating the IOPs of inland water. The Z_{SD} model uses QAA_{v5} to estimate the IOPs; therefore, our hypothesis is that the limiting factor to obtain the Z_{SD} accurately is the estimation of the IOPs. To test this hypothesis, data collected in three field trips were used to apply the Z_{SD} model based on the spectral bands from Operational Land Imager (OLI)/Landsat-8 and multispectral instrument (MSI)/Sentinel-2A sensors. The aim of this work was to evaluate the applicability of the Z_{SD} model to inland water. The specific objectives were: to (1) bio-optically characterize the Nova Avanhandava (Nav) Reservoir; (2) evaluate the performance of the Z_{SD} semi-analytical scheme based on QAA_{v5} using OLI bands and the QAA_{M14} from Mishra et al. (2014) using MSI bands to derive Z_{SD}; and (3) apply the Z_{SD} model to satellite images to retrieve the spatial–temporal distribution of Z_{SD}.

2. Materials and methods

2.1. Study site

Nav is a run-of-river reservoir (Fig. 1) with a mean water level fluctuation lower than 0.50 m year^{-1} (Petesse et al., 2014). Nav is also the fifth of six reservoirs situated along the Tietê River in the western region of São Paulo State, Brazil. The reservoir activity started in 1982, flooding an area of 210 km^2 (at its maximum quota), with a usable volume of 3.8×10^8 m^3, perimeter of 462 km, maximum depth of 30 m, mean water residence time of ~46 days, and an average flow of 688 m^3 s^{-1} (Torloni et al., 1993). The reservoir is part of a region that is influenced by continental tropical and polar Antarctic air masses. The former air mass is hot and dry and occurs mainly during summer (24 °C and 30 °C), while the latter one is cold and damp and despite being active all year, its occurrence is more intense during winter, causing a temperature drop (14 °C to 22 °C; CBH-BT, 2009).

Nav is an oligo- to mesotrophic reservoir with the upper portion of the water column being well oxygenated and pH ranging from slightly acid to alkaline (6.47–8.2), a relatively high conductivity (83–150 μS cm^{-1}), and low concentrations of nutrients (total N: 0.05–0.23 μg l^{-1}, total P: 18.02–32.33 μg l^{-1}; Rodgher et al., 2005; Smith et al., 2014). Together with the high transparency of the water, a favorable environment for submerged macrophyte growth is created (*e.g.*, *Egeria* sp.: *Elodea*; Smith et al., 2014, Rotta et al., 2016). The catchment basin surrounding the reservoir receives input from nonpoint source pollution such as sugarcane and citric plantations (orange and lemon) and cattle breeding.

2.2. Laboratory analysis

The field trips were carried out in austral autumn (Nav1: April 28 to May 2) and austral spring (Nav2: September 23 to 26) of 2014 and austral autumn (Nav3: May 9 and 14) of 2016. The Nav1 and Nav2 field collections resulted in 19 samples each; 18 samples were collected during Nav3 (see Fig. 1 for sampling station locations) following the sample arrangement described in Rodrigues et al. (2016), which consisted of selecting samples randomly taking into account spectrally different regions (stratum) created to cover the bio-optical variability of the reservoir.

Water samples (5 L for each sampling location) were collected just below the air–water interface, filtered on the same day of collection under vacuum pressure through a raw filter or pre-ashed and pre-weighed Whatman GF/F fiberglass filter with a porosity of 0.7 μm, and then frozen (−25 °C) before analysis. Chlorophyll-*a* (Chl-*a*) was extracted with 90% acetone solution and analyzed spectrophotometrically at 663 and 750 nm (Golterman et al., 1978). The suspended particulate matter (SPM) concentration was determined through the method described in APHA (1998); the filters were dried in the oven at 100 °C for 12 h and then weighed using an analytical scale. The inorganic matter was not measured; thus, the equation from Buiteveld (1995) was applied aiming to retrieve the Tripton concentration. A Secchi disk with a diameter of 30 cm was used for Z_{SD} measurements.

To estimate the colored dissolved organic matter (CDOM) absorption coefficient (a_{CDOM}), ~250 mL of water was filtered through a fiberglass Whatman GF/F with a porosity of 0.7 μm and then refiltered under low vacuum pressure using a nylon membrane filter with a porosity of 0.2 μm. The readings were performed using a SHIMADZU UV-2600 UV–VIS spectrophotometer (SHIMADZU, Japan) in absorbance mode. The samples were placed in a 10 cm quartz cuvette (Tilstone et al., 2002). A water volume of 1 L was filtered at low vacuum pressure using a 47 mm diameter fiberglass Whatman GF/F filter. The filters were placed in a brown glass bottle and frozen until analysis. A white filter wetted with ultrapure water was used as reference and the filter containing the particulate was placed on the integrating sphere module of the spectrophotometer with a spectral range from 280 to 800 nm to measure the optical density (OD). The Transmittance–Reflectance (T–R) method described in Tassan and Ferrari (1995, 1998) was employed to derive the total particulate absorption coefficient (a_p). The particulate filter was depigmented by oxidation in 10% sodium hypochlorite (NaClO), ensuring free phytoplankton pigment influence to obtain the

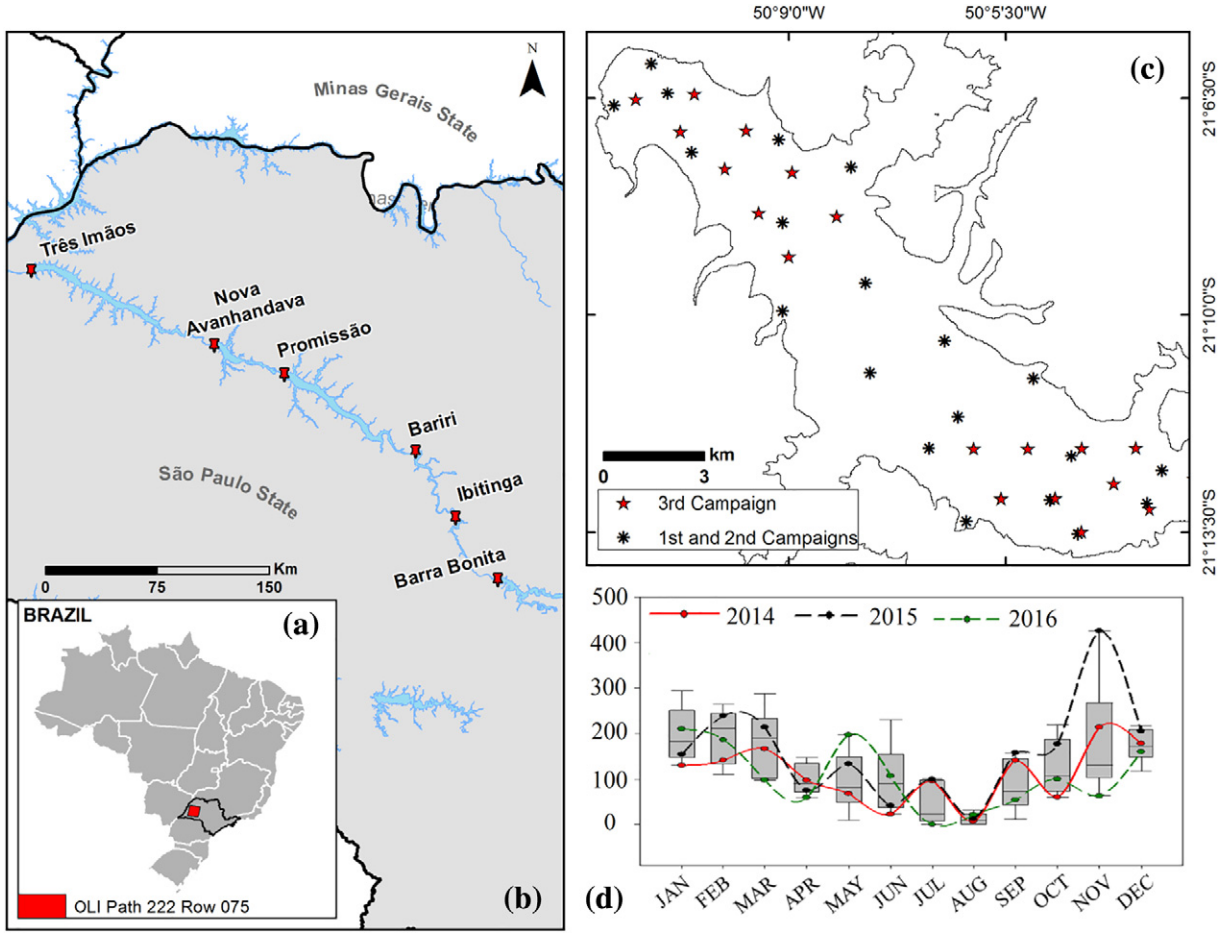

Fig. 1. Maps of the study area emphasizing (a) the territory of Brazil highlighted by the OLI/Landsat-8 scene, (b) the State of São Paulo and the respective reservoirs along the Tietê River starting with Barra Bonita, the first of the cascade followed by the downstream reservoirs of Ibitinga, Bariri, Promissão, Nova Avanhandava (Nav), and Três Irmãos, (c) the sample location in the Nav Reservoir and (d) monthly rainfall (mm) data from NASA's GIOVANNI database for the period of 2011–2016.

non-algal particle (a_{NAP}). The phytoplankton absorption coefficient (a_ϕ) was retrieved by subtracting a_{NAP} from the a_p.

2.3. In situ radiometric data

The above-mentioned surface remote sensing reflectance spectra (R_{rs}; sr^{-1}) were estimated from radiometric measurements taken between 10 am and 2 pm. This procedure was carried out to consider the acquisition geometry based on the time window of light availability during the day (Mobley, 1999). At each sampling station, radiometric measurements were acquired above and below the water surface using hyperspectral radiometers (RAMSES TriOS®; TriOS, Germany) operating in the spectral range between 400 and 900 nm. These radiometric measurements were used to derive the R_{rs} based on Mobley (1999) and K_d. The radiance sensor is equipped with a 7° field-of-view and the irradiance sensor is equipped with a cosine collector. Before being used, the radiometric quantities such as the total upwelling radiance (L_t; $Wm^{-2}\ sr^{-1}\ nm^{-1}$), incident sky radiance (L_s; $Wm^{-2}\ sr^{-1}\ nm^{-1}$), downwelling irradiance incident onto the water surface (E_s; $Wm^{-2}\ sr^{-1}\ nm^{-1}$, and the downwelling irradiance below the water surface (E_d; $Wm^{-2}\ sr^{-1}\ nm^{-1}$) were linearly interpolated to transform the original spectral resolution of ~3.3 nm to 1 nm. This procedure was designed to homogenize the RAMSES measurements because the sensors use different wavelengths.

The sampling rate was ~15 s/sample, resulting in 16 redundancy values for each sampling location. From these measurements, a median value was chosen to represent the spectrum of that location. The acquisition geometry follows the protocol described in Mueller (2000b) and Mobley (1999) to avoid effects of specular radiance and boat shading. During the campaigns, the sky was mostly clear, with few days with partial cloud cover; no whitecaps or foam were observed. In addition, the wind speed did not exceed 6 ms^{-1}. The instruments were positioned on a steel frame; the viewing angle of the L_t and L_s sensors were set to 40° from nadir (zenith) and an azimuth of 90° (from the sun). The K_d value decreases exponentially with depth and is defined as (Mobley, 1994):

$$K_d(z,\lambda) = -\frac{1}{E_d(\lambda)}\frac{dE_d}{dz} \tag{1}$$

Due to changes in the sun illumination, E_d can introduce uncertainties; thus, normalization is required. The definition of E_d according to Mueller (2000b) and Mishra et al. (2005) is presented below:

$$E'_d(z_i,\lambda) = \frac{E_d(z_i,\lambda)E_s(t(z_1),\lambda)}{E_s(t(z_i),\lambda)}, \tag{2}$$

where $E'_d(z_i,\lambda)$ is the normalized E_d at depth z_i; $E_d(z_i,\lambda)$ is the original E_d at depth z_i collected in the field; $E_s(t(z_1),\lambda)$ is E_s at time $t(z_1)$ on the boat during the first scan; and $E_s(t(z_i),\lambda)$ is E_s measured from the roof of the boat at time $t(z_i)$.

The best approximation of the R_{rs} values was calculated from the radiometric quantities collected at the water surface as follows:

$$R_{rs}(\lambda) = \frac{L_t(\lambda) - L_{SR}(\lambda)}{E_d(\lambda)} = \frac{L_t(\lambda) - \left(\rho_{sky} \times L_s(\lambda)\right)}{E_d(\lambda)} - \Delta, \tag{3}$$

where $L_{SR}(\lambda)$ is the surface-reflected light and consists of a fraction ($\rho_{sky} \approx 0.02 - 0.05$) of $L_s(\lambda)$ and the sun glint, residual glint, whitecaps, and foam-reflected light (Δ; Yan and Sydor, 2006, Lee et al., 2010; Garaba et al., 2015). The Δ value can be assumed to be zero for oceanic water in the near-infrared (NIR); however, in turbid water, this element must be retrieved. The absorption by SPM decreases to almost zero beyond 700 nm; the increase of its concentration creates a gradient in the NIR of R_{rs} due to particle scattering (Dekker, 1993; Yang et al., 2013). As reported by Lee et al. (2010), Δ can be estimated after modeling R_{rs} as a function of the spectral IOPs; it can be compared with R_{rs} derived from the equation below:

$$R_{rs}(\lambda) \approx T_{rs}(\lambda) - F \times S_{rs}(\lambda) - \Delta, \tag{4}$$

where $T_{rs}(\lambda)$ is the total remote sensing reflectance, F is the surface Fresnel reflectance based on the viewing geometry (~0.021), and $S_{rs}(\lambda)$ is the sky remote sensing reflectance. The value of Δ is then numerically derived by spectral optimization that minimizes the error between the modeled R_{rs} and optimized R_{rs} (Lee et al., 2010).

The R_{rs} is the input for the models to retrieve the optically significant constituent (OSCs) concentration. However, it is necessary to match the hyperspectral data with those from satellite data by convoluting the spectral response functions of both the MSI from Sentinel-2 and OLI from Landsat-8 bands to derive band-weighted reflectance data (Gordon, 1995):

$$R_{rs}^{MSI,OLI}(\lambda_k) = \frac{\int_{\lambda_i}^{\lambda_j} S(\lambda) R_{rs}(\lambda)}{\int_{\lambda_i}^{\lambda_j} S(\lambda)}, \tag{5}$$

where $R_{rs}^{MSI,OLI}$ stands for the remote sensing reflectance convoluted from MSI or OLI spectral bands; λ_i and λ_j are the lower and upper limit of the band λ_k, respectively; and $S(\lambda)$ is the spectral response function of the ith spectral band of MSI (ESA, 2016) or OLI (Barsi et al., 2014).

2.4. Z_{SD} modeling

To retrieve Z_{SD} using the semi-analytical model of Lee et al. (2015), three steps are required (Fig. 2): i) the first one (M1) is based on the estimation of the IOPs, a and b_b, using version 5 of QAA (QAA_{v5}); ii) the second step (M2) is the estimation of K_d based on a and b_b, and iii) the third step (M3) is the retrieval of Z_{SD} based on K_d and R_{rs}.

In the following section, we will show how Lee et al. (2015) used these three models (M1, M2, and M3) to estimate the Z_{SD}.

2.4.1. Model M1 — estimating IOPs from QAA

The QAA approach was successfully applied to optically deep water to estimate the IOPs, assuming $a(440) < 0.3\ m^{-1}$ (Lee et al., 2002). However, modifications were carried out to better describe the particularities of turbid inland water (Lee et al., 2009; Yang et al., 2013; Mishra et al., 2014). Aiming to retrieve a and b_b, Lee et al. (2002) described six steps mixing empirical and analytical approaches. The models of Lee et al. (2009) and Mishra et al. (2014) followed the same steps; however, some issues were considered such as the choice of the reference wavelength and the empirical determination of the coefficients in step 2 (see Table 1). For turbid water with high absorption coefficients, the previous studies showed that the reference band must be shifted to longer wavelengths, such as the NIR region, once the contribution of other OCSs, such as SPM, is higher than that of water (Lee et al., 2009). In a recent study of Li et al. (2016), the estimated absorption coefficients at 550 and 675 nm were improved using 700 nm as reference band because the water quality of the Songhua Lake, China (SPM average of 3.32 mg l^{-1} and Chl-a average of 6.35 mg m^{-3} during summer) exhibited values characteristic of ocean and coastal water for which the original algorithm was developed.

Different QAA approaches were evaluated considering the reference wavelength from Lee et al. (2009) and Mishra et al. (2014). The QAA_{v5} model used the bands from OLI/Landsat-8, while the latter one, called QAA_{M14}, used the bands from MSI/Sentinel-2 because the reference wavelength at 705 nm is available in the satellite setting.

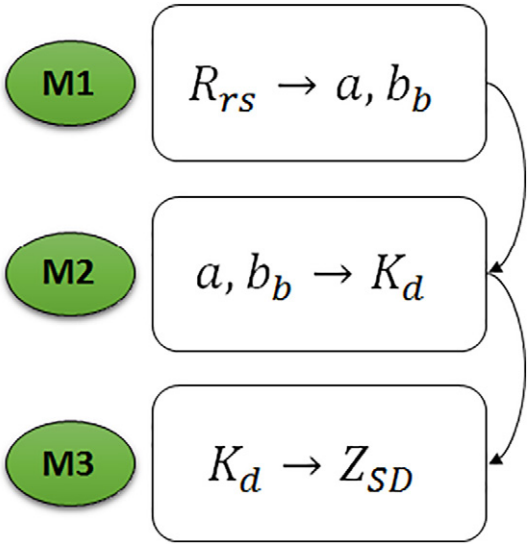

Fig. 2. Flowchart showing the steps M1, M2, and M3 for retrieving Z_{SD} using the mechanistic model from Lee et al. (2015).

Fukushima et al. (2015) used a semi-analytical model to estimate Z_{SD} based on IOPs retrieved by QAA_{v5} and QAA_turbid from Yang et al. (2013) in 10 lakes in Japan. The parameter used to select each QAA configuration was based on the type of water (clear or turbid). Considering that the turbidity does not vary in Nav (from clear to turbid), only one approach was applied for the entire reservoir. The model based on Yang et al. (2013) was also tested; however, after error analysis (not shown here), the QAA_{M14} showed a slight advantage over the first one.

2.4.2. Model M2 — estimating K_d from IOPs

The semi-analytical approach for K_d retrieval was presented by Lee et al. (2013); the IOPs were derived through.

$$K_d(\lambda) = (1 + m_0 \times \theta_s) a(\lambda) + \left(1 - \gamma \frac{b_{bw}(\lambda)}{b_b(\lambda)}\right) \times m_1 \times \left(1 - m_2 \times e^{-m_3 \times a(\lambda)}\right) b_b(\lambda), \tag{6}$$

where θ_s is the solar zenith angle, here considered to be 30°; m_{0-3} and γ are equal to 0.005, 4.26, 0.52, 10.8, and 0.265, respectively; $b_{bw}(\lambda)$ is the backscattering coefficient for water molecules based on Smith and Baker (1981); and a and b_b are notations for total absorption and backscattering coefficients, respectively. This algorithm is based on the IOPs and can be retrieved analytically through QAA (Lee et al., 2002). The coefficients of Eq. (6) were originally derived by Lee et al. (2013) using Hydrolight (Mobley, 1995) simulations on oligotrophic waters (the Chl-a concentrations were set to 0.01, 0.02, 0.05, and 0.1 mg m^{-3}) and the Case-1 models of Morel and Maritorena (2001) for optical properties (Lee et al., 2013).

2.4.3. Model M3 — estimating Z_{SD} from K_d and R_{rs}

Based on the results from M1 and M2, the Z_{SD} is retrieved as:

$$Z_{SD} = \frac{1}{2.5\ Min(K_d^{tr})} \ln\left(\frac{|0.14 - R_{rs}^{tr}|}{0.013}\right), \tag{7}$$

where K_d^{tr} is the diffuse attenuation coefficient of the downwelling irradiance in the transparent spectral window and here represents the minimum value within the visible domain (443–665 nm); similar to Lee et al. (2016), the green band was chosen to represent this minimum value.

Table 1
QAA steps following version 5 from Lee et al. (2009), termed QAA_{v5}, and the version from Mishra et al. (2014), named QAA_{M14}, considering highly turbid water; b_b is defined as $b_b = b_{bw} + b_{bp}$.

Step	Property	QAA_{v5}	QAA_{M14}
0	r_{rs}	$= R_{rs}/(0.52 + 1.7R_{rs})$	Same
1	$u(\lambda)$	$= \frac{-g_0 + \sqrt{+\left[(g_0)^2 + 4g_1 r_{rs}(\lambda)\right]}}{2g_1}$	Same
2	$a(\lambda_0)$	$= \log\left(\frac{r_{rs}(\lambda_1) + r_{rs}(\lambda_2)}{r_{rs}(\lambda_0) + 5 \times \frac{r_{rs}(\lambda_3)}{r_{rs}(\lambda_2)} \times r_{rs}(\lambda_3)}\right)$	$= \log\left(\frac{0.01 \times r_{rs}(\lambda_1) + r_{rs}(\lambda_2)}{r_{rs}(\lambda_0) + 0.005 \times \frac{r_{rs}(\lambda_2)}{r_{rs}(\lambda_1)} \times r_{rs}(\lambda_2)}\right)$
		$a(\lambda_0) = a_w(\lambda_0) + 10^{-1.146 - 1.366\chi - 0.469\chi^2}$ $(\lambda_0 = 55x; \lambda_1 = 443; \lambda_2 = 490; \lambda_3 = 667)$	$a(\lambda_0) = a_w(\lambda_0) + 10^{-0.7153 - 2.054\chi - 1.047\chi^2}$ $(\lambda_0 = 708; \lambda_1 = 443; \lambda_2 = 620)$
3	$b_{bp}(\lambda_0)$	$= \frac{u(\lambda_0)a(\lambda_0)}{1 - u(\lambda_0)} - b_{bw}(\lambda_0)$	Same
4	η	$= 2.0\left\{1 - 1.2\exp\left[-0.9\frac{r_{rs}(443)}{r_{rs}(555)}\right]\right\}$	Same
5	$b_{bp}(\lambda)$	$= b_{bp}(\lambda_0)\left(\frac{\lambda_0}{\lambda}\right)^{\eta}$	Same
6	$a(\lambda)$	$= \frac{[1 - u(\lambda)][b_{bw}(\lambda) + b_{bp}(\lambda)]}{u(\lambda)}$	Same

According to Buiteveld (1995), the maximum transmission of light happens in the green region in eutrophic water, which is due to the selective absorption in the blue and red spectral regions. The R_{rs}^{tr} parameter represents the remote sensing reflectance of this wavelength.

The spatial distribution of Z_{SD} will be obtained by applying the semi-analytical scheme to a time series of OLI/Landsat-8 images; the first step is to use the most appropriate atmospheric correction method for our study area.

2.5. OLI/Landsat-8 atmospheric correction and acquisition

The application of imagery data to retrieve information about waterbodies requires high-quality atmospheric correction. Franz et al. (2015) used SeaDAS (version 7.2) and concluded that OLI/Landsat-8 imagery has enough attributes to support the standard atmospheric correction approach developed by NASA's global ocean color missions; in addition, it determines and removes aerosol contributions by comparison with real aerosol models derived by OLI/NIR and SWIR information. Classical methods, such as Fast Line-of-sight Atmospheric Analysis of Hypercubes (FLAASH) and Atmospheric and Topographic Correction for Satellite Images (ATCOR), were tested due to their simplicity of use and reasonable success in retrieving OSCs of inland water (Kutser et al., 2016; Kong et al., 2015). The ACOLITE, which is an atmospheric correction and processor for the OLI/Landsat-8 and MSI/Sentinel-2 data, was also evaluated once this approach was created to meet aquatic environments (Vanhellemont and Ruddick, 2014, 2015). Recently, the provisional Landsat 8 Surface Reflectance (L8SR) product, which is produced using a specialized software and acquired through the Earth Explorer on-demand service, has been applied to aquatic environments to retrieve water quality parameters (USGS, 2016; Yunus et al., 2015, Concha and Schott, 2016; Pahlevan et al., 2017). The OLI/Landsat-8 image from May 4, 2014, was used for atmospheric correction validation and sixteen images covering the years of 2014 and 2016 (Path 222, Row 075) were evaluated for long-term analysis. The images were acquired from the United States Geological Survey website (http://earthexplorer.usgs.gov/).

2.6. Long-term trend of Z_{SD}

The long-term Z_{SD} dynamics in Nav were analyzed considering all images available from 2014 and 2016. The criteria used for data selection were based on cloud free OLI/Landsat-8 images. Thus, eight images were downloaded for each year. The available months for 2014 were January, February, April, May, July, August, September, and December, while those for 2016 were January, February, March, April, June, July, August, and October. Atmospherically corrected images were used to create the long-term map.

2.7. Accuracy assessment

To retrieve Z_{SD} values of Nav, the semi-analytical scheme described by Lee et al. (2015) was used and the simulated R_{rs} data from the MSI and OLI sensors were applied as input. Once the main goal was to verify the accuracy of the original model to retrieve Z_{SD} of inland water, such as Nav, which is an oligo- to mesotrophic reservoir, data from three field trips were used. Six samples from Nav1 were employed to validate the model based on satellite data. The OLI/Landsat-8 image was acquired on May 4, 2014 (Path 222, Row 075), and the samples were collected on May, 1–2, 2014. The same procedure could not be accomplished using MSI/Sentinel-2 data due to the absence of data for a date closely matching the field data collection.

The statistical indicators used for validation were the total RMSD, bias, and MAPE. To provide a broader statistical overview of the error, the normalized bias (B^*), normalized standard deviation (σ^*), linear correlation (R), and normalized unbiased RMSD ($uRMSD^*$) were also applied. The term "normalized" stands for all statistical metrics divided by the standard deviation of the reference, here named σ_{meas}, while the term "unbiased" emphasizes that the measure removes any information about the potential bias; σ^* and R represent the magnitude of data

dispersion and shape patterns. To obtain ideal conditions, the magnitude and shape might assume $\sigma^* = R = 1$, which leads to the minimum *uRMSD**.

A different perspective about the contribution of the error was achieved using the Taylor and Target diagrams (Taylor, 2001; Jolliff et al., 2009). In the polar coordinate diagram (Taylor graphic), the radial (along-axis) distance from the origin is related to σ^* and the angular position corresponds to *R*. The distance between the reference and the modeled points is proportional to *uRMSD**. The observation is the reference point, which is indicated by the polar coordinates (1.0, 1.0) when the metrics are normalized. The target diagram considers the Cartesian plane (*uRMSD**, *B**), where *uRMSD** > 0 means that the model standard deviation is larger than the reference, while *uRMSD** < 0 indicates the contrary; *B** > 0 signifies positive bias, while *B** < 0 indicates negative bias. The distance from the origin to the model value is defined by the normalized total RMSD (*RMSD**). A circle is created to represent *RMSD** = 1.0 and the model values falling inside the circle (total RMSD values less than the σ_{meas}) tend to provide a better estimate than the mean of the observations (Friedrichs et al., 2009).

$$RMSD = \sqrt{\frac{1}{n}\sum_{i=1}^{n}\left(x_{est,i} - x_{meas,i}\right)^2} \tag{8}$$

$$MAPE = \frac{100\%}{n}\sum_{i=1}^{n}\left|\frac{x_{est,i} - x_{meas,i}}{x_{meas,i}}\right| \tag{9}$$

$$\text{bias} = \frac{1}{n}\sum_{i=1}^{n}\left(x_{est,i} - x_{meas,i}\right) \tag{10}$$

$$B^* = \left(\frac{\overline{x}_{est} - \overline{x}_{meas}}{\sigma_{meas}}\right) \tag{11}$$

$$\sigma^* = \frac{\sigma_{est}}{\sigma_{meas}} \tag{12}$$

$$RMSD^* = \frac{RMSD}{\sigma_{meas}} \tag{13}$$

$$uRMSD^* = sign(\sigma_{est} - \sigma_{meas})\sqrt{1 + \sigma^{*2} - 2\sigma^* R}, \tag{14}$$

where *n* is the number of samples $x_{est,i}$ and $x_{meas,i}$ represent the estimated and measured values, respectively; $\overline{x}_{est}$ and $\overline{x}_{meas}$ represent the averages of the estimated and measured values, respectively; and σ_{meas} and σ_{est} are the standard deviation of the measured and estimated values, respectively.

3. Results

3.1. Biogeochemical and optical characterization

The water quality parameters are displayed in Table 2. The table shows how homogenous the data are, except when compared with those from Nav3. The data from 2014 does not show statistical differences between austral autumn an austral spring, exhibiting seasonal independence. However, considering the data collected in 2016, the variables show a statistical change, indicating the impact of rainfall conditions on the water quality (see Fig. 1d for rainfall data).

The SPM and Chl-*a* concentrations from all field trips are peculiar for an oligo- to mesotrophic environment. The averages between Nav1 and Nav2 did not show statistical differences for SPM, turbidity, tripton, and Z_{SD} ($p > 0.05$); however, the contrary was observed for the Chl-*a* concentration ($p < 0.05$). The SPM and Chl-*a* averages related to Nav1 and Nav2 were statistically different from that of Nav3 ($p < 0.05$). In addition, the average Z_{SD} and tripton for Nav1 did not statistically differ from that of Nav3; however, the contrary was the case for Nav2 and Nav3. These results imply that some factor led to the differentiation of the water quality from 2014 to 2016; according to Coelho et al. (2015), southeastern Brazil experienced a major drought event in 2014, affecting the water quality and availability in this region. In 2016, the precipitation rate led to the increase of the surface runoff and therefore the input of sediment load into the reservoir.

Table 2
Descriptive statistics from three field trips carried out in Nav (the notations in the table stand for: Aver–average, SD–standard deviation, Min–Max–minimum–maximum, CV–coefficient of variation). Tripton was measured based on Buiteveld (1995), where Tripton = SPM − 0.07Chl − *a*.

		Nav1 ($n = 19$)	Nav2 ($n = 19$)	Nav3 ($n = 18$)
SPM (mg l^{-1})	Aver ± SD	1.00 ± 0.64*	1.00 ± 0.58	2.83 ± 0.65**
	Min–max	0.10–2.60*	0.50–2.80	1.87–3.67**
	CV (%)	63.96*	57.73	23.12**
Chl-*a* (μg l^{-1})	Aver ± SD	6.30 ± 2.53	9.01 ± 4.21	26.56 ± 7.03**
	Min–max	2.46–12.56	4.51–20.48	15.84–38.59**
	CV (%)	40.12	46.76	26.49**
Tripton	Aver ± SD	0.66 ± 0.53*	0.52 ± 0.50	0.97 ± 0.40**
	Min–max	0.10–2.15*	0.09–2.04	0.37–1.76**
	CV (%)	79.34*	96.53	40.79**
Turbidity (NTU)	Aver ± SD	1.63 ± 0.42	1.73 ± 0.41	–
	Min–max	1.01–2.47	1.01–2.56	–
	CV (%)	25.45	23.55	–
Z_{SD}(m)	Aver ± SD	3.19 ± 0.62	3.41 ± 0.62	2.97 ± 0.63
	Min–max	2.29–4.80	2.45–4.65	1.91–3.80
	CV (%)	19.44	18.07	21.03
a(443) (m^{-1})	Aver ± SD	0.75 ± 0.12	0.80 ± 0.22	0.99 ± 0.18
	Min–max	0.49–1.06	0.42–1.45	0.65–1.37
	CV (%)	16.13	27.77	18.30
a_ϕ(m^{-1})	Aver ± SD	0.17 ± 0.07	0.24 ± 0.09	0.29 ± 0.13
	Min–max	0.10–0.38	0.10–0.43	0.11–0.57
	CV (%)	39.97	35.98	44.87

* $n = 16$.
** $n = 09$.

The abundance of phytoplankton is generally higher during dry periods (austral winter/spring), probably caused by the decrease of the river input, relatively high water temperature, and increase of water residence time and light availability (Wang et al., 2010; Curtarelli et al., 2015). In Nav3, for example, the Chl-*a* concentration increased considerably compared with Nav1 and Nav2. This can be explained by the dry period established in March and April of 2016, depicting values even lower than 2014, that created a favorable environment for phytoplankton growth. In the data collection month (May 2016), the rainfall started to increase, reaching the highest value since 2011; thus, Chl-*a* reduction was expected due to light limitations and the dilution effect (Watanabe et al., 2016b).

The IOPs provide information about the contribution and dominance of certain OSCs in the water and also assist in the estimation of these components using proper algorithms (Mishra et al., 2014; Riddick et al., 2015). The proportion of each IOP in detriment to the total absorption budget, except for the water contribution (a_{t-w}), was computed considering the wavelengths of OLI bands (443, 560 and 655 nm). The absorption of Nav1 was represented by the NAP at 443 and 560 nm of with 42.90% ± 6.51% and 48.69% ± 7.61%, respectively. At 655 nm, the phytoplankton contributed with 48.69% ± 7.61%, highlighting the high variability of the inland water composition (Fig. 3a–c). Regarding Nav2, CDOM contributed with 40.44% ± 8.39% at 443 nm, followed by NAP with 46.00% ± 9.68% at 560 nm and 46.88% ± 10.69% at 655 nm. Nav3 had a NAP dominating the blue and green wavelengths of 62.74% ± 9.31% and 71.68% ± 13.13%, respectively. At 655 nm, the phytoplankton achieved 53.86% ± 13.67% of the a_{t-w}. Nav1 and Nav3 were characterized by the predominance of a_ϕ at 655 nm, which is considered a typical diagnostic feature of phytoplankton attributed to the backscattering by CDOM (Gitelson, 1992).

At all wavelengths, Nav3 presented the lowest percentage of CDOM (<10%). The allochthonous organic matter basically originated from terrestrial plants; however, it is worth mentioning that Nav is surrounded

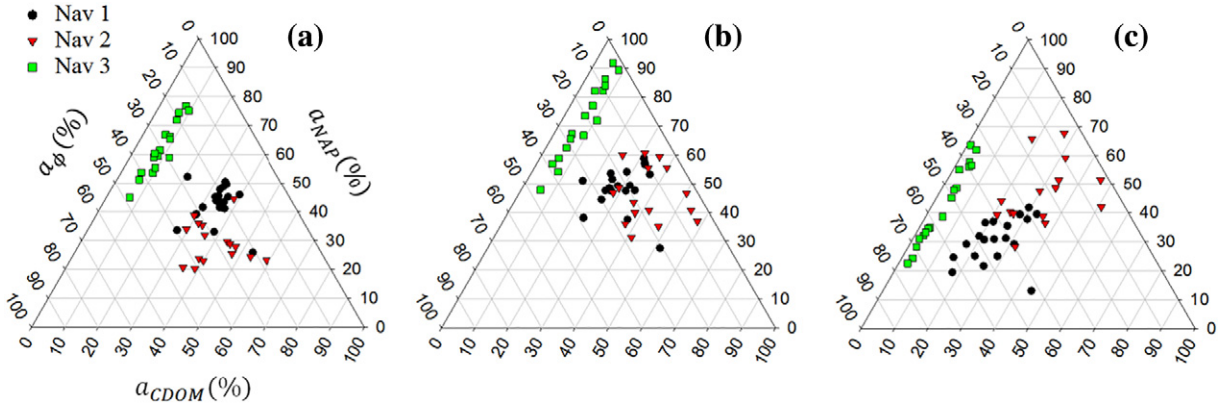

Fig. 3. Ternary plots depicting the relative contribution of a_{CDOM}, a_{NAP}, and a_ϕ at (a) 443, (b) 560, and (c) 655 nm.

by sugar cane, citrus plantations, and bare soil. After rainfall events, the runoff carries mostly inorganic matter, which can also be observed in the ternary plots based on the predominance of NAP in the blue–green spectral region (Fig. 3). The water level of the reservoir does not vary significantly; thus, the vegetation near the waterbody is not flooded, limiting the production of dissolved organic matter (DOM). In addition, the shoreline is basically sand with less influence of clay (Cavenaghi et al., 2003). Gücker et al. (2016) reported that dissolved organic carbon (DOC) concentrations are higher in urban streams when compared with pasture, natural and agriculture streams. The two months that preceded Nav3 showed the lowest rainfall data considering the period between 2011 and 2016; therefore, limited input entered the reservoir.

The R_{rs} spectra are quite similar, presenting absorption and reflectance features typical for inland water (Fig. 4). The spectral range between 400 and 750 nm was chosen to display the main features for the three time periods. The reflectance peak at ~550 nm is related to the weak absorption of chlorophyll and high contribution of particulate backscattering. The feature near 630 nm is related to phycocyanin absorption (Cheng et al., 2013). A smooth absorption feature near 675 nm represents the absorption of chlorophyll. At longer wavelengths (>650 nm), pure water starts to strongly absorb, while the scattering of particulate influences the reflectance (Yacobi et al., 2011). Overall, the spectral features did not change much from one field trip to another; the main change was the magnitude of reflectance near 560 nm between Nav1 and Nav3 and Nav2 and Nav3 ($p < 0.05$). The coefficient of variation (CV%) with respect to the wavelengths of 443, 560, and 655 nm was higher for Nav2 (61%, 51%, and 57%, respectively) and lower for Nav1 (25%, 28%, and 35%, respectively), while Nav3 showed intermediary values (34%, 49%, and 51%, respectively). This variability is intrinsically related to the water composition of Nav and can be directly linked to the various uncorrelated constituents that are dissolved or suspended in the water for which the relative concentrations change accordingly to different biological and physical processes (Lubac and Loisel, 2007). In addition, previous studies revealed that the variance is mostly based on particulate backscattering (b_{bp}) and less on dissolved absorption (Toole and Siegel, 2001; Lubac and Loisel, 2007).

3.2. Implication of M1 for M2 and M3 accuracy

To check the performance of K_d and the Z_{SD} model, R_{rs} data from three different dates were used as input (except for K_d, which only included *in situ* data from Nav1 and Nav2). The a and b_b coefficients were analytically derived from QAA_{v5} and QAA_{M14} and further applied to satellite data to retrieve Z_{SD}. Considering the limited number of bands from OLI/Landsat-8 and the absence of a band near 708 nm, which is highly recommended for studies of inland water, the IOPs were derived using QAA_{v5} (see Table 1). The QAA version 6 was also analyzed; however, the results were not suitable to retrieve Z_{SD} and therefore are not presented here. The QAA_{M14} using MSI/Sentinel-2 bands was used to evaluate the performance of a productive turbid water model. The model followed the original steps including the coefficients without reparameterization; however, two bands were replaced due to the absence of bands 620 and 708 nm in MSI/Sentinel-2 images. By relating the hyperspectral band at 620 nm to $R_{rs}^{MSI}(665)$ and 708 nm to $R_{rs}^{MSI}(705)$, high determination coefficients ($R^2 = 0.9856$ and $R^2 = 0.9995$, $p < 0.05$, $n = 56$, respectively) and low relative percentage errors (27.23% and 12.04%, $n = 56$, respectively) were obtained, indicating that both bands were suitable to replace the original ones.

The estimation of K_d depends on the inversion of a and b_b from accurate R_{rs} values. Yang et al. (2014) observed that when using QAA_{v5} to provide the IOPs for a turbid lake in Japan, the $K_d(443, 556, 669)$ measures based on Lee et al. (2005b) were underestimated, producing high errors (relative error, RE = 66.80%). However, the result improved (RE = 22.33%) when they shifted the reference wavelength to 754 nm, but not as much as using QAA_turbid from Yang et al. (2013), which showed a better accuracy (RE = 12.96%). The authors also evaluated QAA_{v6}. However, this approach led to an increased error (RE = 75.05%). In the current study, a direct validation between estimated and measured b_b was not performed; data from Nav1 and Nav2 presented *in situ* data for K_d.

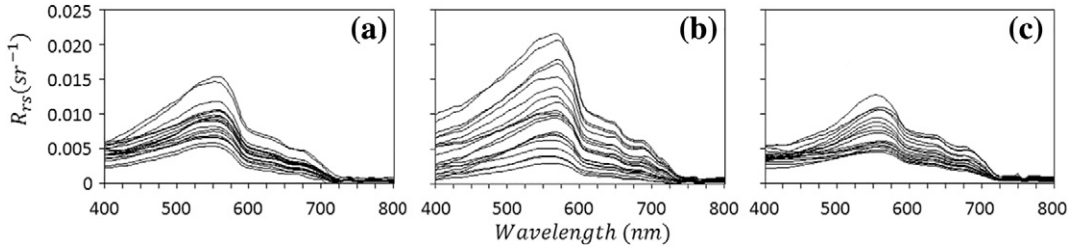

Fig. 4. R_{rs} of the three field trips carried out in 2014 and 2016: (a) Nav 1, austral autumn 2014; (b) Nav 2, austral spring 2014; and (c) Nav3, austral autumn 2016.

The K_d based on QAA_{v5} (here named K_{dv5}) is displayed in Fig. 5a; the value based on QAA_{M14} (here termed K_{dM14}) is displayed in Fig. 5b.

The agreement between estimated and measured $K_d(561)$ using QAA_{v5} was better in Nav1 than in Nav2, which exhibited more disperse data. The K_{dM14} produced high variability for both Nav1 and Nav2, also depicting high uncertainties. The RMSD, MAPE, and bias were 0.05 m^{-1}, 10.35%, and −0.02 m^{-1} for Nav1 using K_{dv5} and 0.06 m^{-1}, 12.68%, and −0.03 m^{-1} using K_{dM14}, respectively, while Nav2 yielded low accuracies using both methods such as 0.09 m^{-1}, 19.76%, and 0.00 m^{-1} for K_{dv5} and 0.13 m^{-1}, 28.29%, and −0.04 m^{-1} for K_{dM14} (Fig. 5c). Yang et al. (2014) used *in situ* a and b_b values to retrieve K_d based on Lee et al. (2005b) and found an agreement between the estimated and measured $K_d(556)$ of 86%, with a RE of 8.34%. However, when they used QAA_{v5}, the agreement dropped to 10%, with a RE of 66.06%. To overcome the poor performance of the model, they switched the QAA approach to QAA_turbid, which increased the performance to 56%, with a RE of 16.42%.

Z_{SD} results from QAA_{v5} (here named Z_{SDv5}) based on OLI/Landsat-8 bands are displayed in Fig. 5d. The values from all three field trips did not show a good agreement between estimated and measured Z_{SD}; the worst performance was observed in Nav2, followed by Nav3. The three datasets were underestimated; however, the values did not scatter as much as the ones retrieved from QAA_{M14} (here named Z_{SDM14}).

The errors obtained from the use of Z_{SDv5} are shown in Fig. 5e (Nav1: RMSD = 0.55 m, MAPE = 12.86%, and bias = −0.35 m; Nav2: RMSD = 1.18 m, MAPE = 28.83%, and bias = −1.00 m; Nav3: RMSD = 0.99 m, MAPE = 31.17%, and bias = −0.90 m). The results presented in Lee et al. (2016) showed that the semi-analytical model achieved a R^2 of 0.96 using OLI/Landsat-8 bands for a Z_{SD} ranging between ~0.1 and 30 m in seawater and an average unbiased absolute percentage difference of 16.7% and 18.2% using data covering different regions including inland water (Lee et al., 2015). Al Kaabi et al. (2016) applied the empirical relationship between Z_{SD} and $1/K_d(490)$ based on Lee et al. (2005a) and obtained a R^2 of 0.62 and RSMD of 26.68% for the Arabian Gulf. These results highlight the success of the semi-analytical approach over the empirical model; however, the method used in Lee et al. (2015) did not show the same accuracy for Nav, which is probably related to the input data originating from model M1 (see Fig. 2), as observed in Fig. 5.

The performance of K_d and Z_{SD} is highly affected by the estimation of IOPs from QAA; according to Li et al. (2016), the success for inland water demands the shifting of the reference band to longer wavelengths (700 nm) and a high contribution of $a_{CDOM}(443)$ to $a(\lambda)$. The high influence of $a_{NAP}(440)$ can lead to a poor accuracy of the algorithm. The authors observed a contribution of CDOM of >70% to $a(\lambda)$ in the Songhua Lake, China, which has water quality parameters very close to that of Nav. In Nav, the slight dominance of NAP in $a_{t-w}(443)$ is evident, except for Nav2, which showed a CDOM with a proportion of 40%, followed by phytoplankton with 30% (Fig. 3). Thus, different from Li et al. (2016), the total absorption budget was balanced between the absorption coefficients, making it difficult to achieve a good performance with QAA. In addition, the authors also drew attention to the need of large amounts of seasonal and regional information to calibrate the model in different water types.

Fig. 5e shows that most of Z_{SD} values retrieved by Z_{SDM14} were underestimated, showing that the model was not suitable to map this variable using this setting. The errors for Z_{SDM14} exceeded the uncertainties of Z_{SDv5} (Nav1: RMSD = 0.70 m, MAPE = 14.33%, and bias = −0.26 m; Nav2: RMSD = 1.50 m, MAPE = 35.94%, and bias = −0.35 m; and Nav3: RMSD = 1.26 m, MAPE = 39.13%, and bias = −1.19 m). The QAA_{M14} was designed for very turbid cyanobacteria-dominated water with high $a_\phi(443)$ ranging between 3.44 and 47.21 m^{-1}, representing >54% of $a(443)$. This scenario is very different from that in Nav with $a_\phi(443) < 0.57\ m^{-1}$. To retrieve $a(\lambda)$, Mishra et al. (2014) shifted the reference wavelength to 708 nm and the band combination in step 2 (Table 1) included the band at 620 nm, which is a diagnostic feature for phycocyanin (Simis et al., 2005). In addition to QAA_{M14}, many other efforts have been made to study inland water (Le et al., 2009; Yang et al., 2013; Li et al., 2016). However, most of them focused on very turbid water with high absorption coefficients. As presented here, these types of approaches were not suitable to derive IOPs in a waterbody with $a(443) < 1.45\ m^{-1}$ and the consequence is propagated to the Z_{SD} values. In addition, Yang et al. (2014) showed

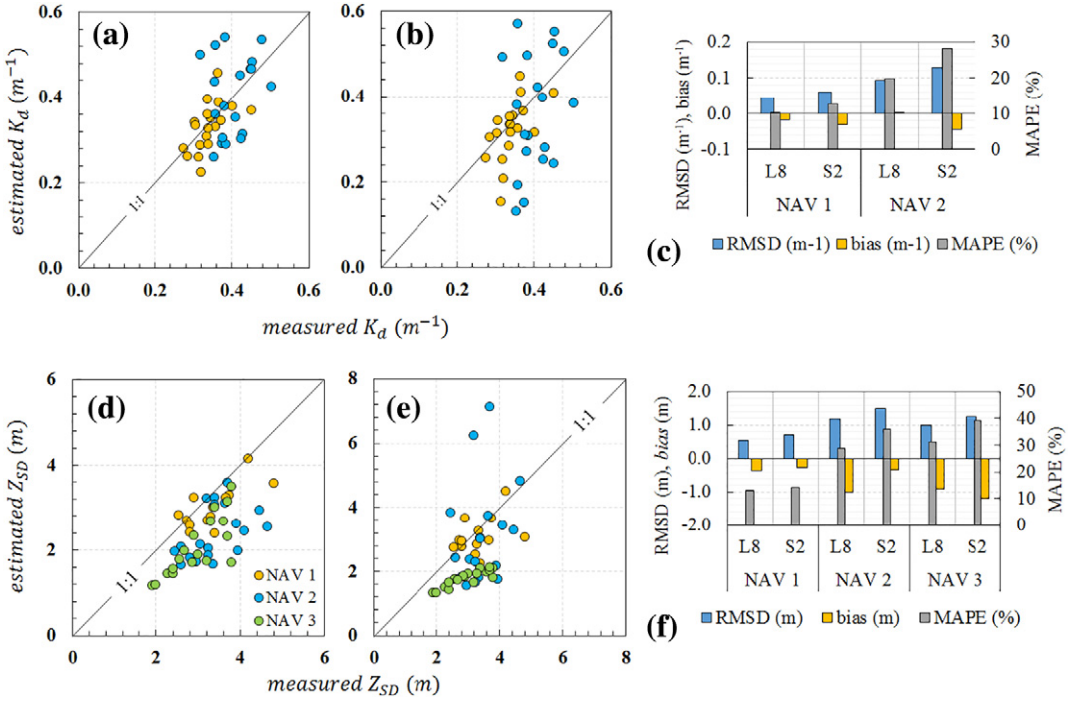

Fig. 5. Comparison between estimated and measured $K_d(561)$ values using: (a) K_{dv5} and (b) K_{dM14}. (c) Uncertainties of K_d represented by RMSD (m), bias (m), and MAPE (%). Z_{SD} values using: (d) Z_{SDv5} and (e) Z_{SDM14}. (f) Uncertainties of Z_{SD} represented by RMSD (m), bias (m), and MAPE (%); L8 and S2 stand for OLI/Landsat-8 and MSI/Sentinel-2, respectively.

that, even when shifting the reference wavelength to longer wavelengths, the improvement in the IOP estimation would be compromised due to the spectral slope (η) of b_{bp} that also affects the estimation of IOPs. Therefore, we proposed to change the empirical steps of QAA_{v5} to reduce the errors in estimating the IOPs and consequently improve the performance of the Z_{SD} model.

3.3. Improvement of M1 for M2 and M3 modeling

As shown previously, the QAA version led to different performances of the K_d and Z_{SD} models, with a slight advantage of Z_{SDv5} over Z_{SDM14}. Therefore, the estimation of Z_{SD} can be improved by recalibrating the empirical steps of QAA_{v5}. The same band combinations of all steps were maintained and one factor (C_1) was included in the numerator of χ; the factor of the denominator (C_2) was then changed (Table 1) to retrieve $a(\lambda_0)$, similar to Mishra et al. (2014), aiming to move the Z_{SD} data upwards closer to the 1:1 line because the estimated values showed an underestimation pattern (Eq. (15)).

$$\chi = log\left(\frac{C_1 \times r_{rs}(\lambda_1) + r_{rs}(\lambda_2)}{r_{rs}(\lambda_0) + C_2 \times \frac{r_{rs}(\lambda_3)}{r_{rs}(\lambda_2)} \times r_{rs}(\lambda_3)}\right), \quad (15)$$

This step is important because it includes the $a(\lambda_0)$ estimation. If this procedure fails, the error will be propagated to the next step [*e.g.*, the estimation of $b_b(\lambda_0)$]. To estimate $b_{bp}(\lambda)$ accurately, $b_b(\lambda_0)$ and η are needed. The parameter η (step 4, Table 1) was modeled empirically using data from the NOMAD dataset with sampling sites in the open ocean and coastal water (Yang et al., 2013). Therefore, step 4 was also changed by replacing the value 2 by 2.2, similar to Lee et al. (2002). It is noteworthy that *in situ* IOPs were not used for QAA improvement; instead, the final K_d and Z_{SD} retrieved by the semi-analytical model were compared with *in situ* data.

After a simple optimization, the values of C_1 and C_2 were assigned to 0.02 and 0.005, respectively. The IOPs were further converted to K_d, considering the sun zenith angle at the time of observation of each sampling location. As result, the uncertainties of K_d of the new version (here named K_{dR17}) related to Nav1 and Nav2 slightly improved and showed a MAPE of 8.89% and 18.76%, respectively (Fig. 6a, b). The improvement was also propagated to the Z_{SD} retrieval (Z_{SDR17}). The uncertainties diminished for Nav1, Nav2, and Nav3; however, data from Nav2 were more dispersed, leading to an underestimation of Z_{SD} (Fig. 6c, d).

The R^2 of Nav1 increased to 0.65 and the RMSD and MAPE decreased to 0.52 m and 11.71%, respectively. Nav2 also showed improvements; however, not as significant as that of the other two field campaigns. The R^2 was 0.19, while RMSD and MAPE decreased to 0.90 m and 19.75%, respectively. The R^2 of Nav3 was 0.75 and the RMSD and MAPE were 0.32 m and 8.65%, respectively.

The only difference between the native scheme of Z_{SDv5} and Z_{SDR17} is the replacement of QAA_{v5} by the improved QAA_{R17} to estimate $a(561)$ and $b_b(561)$. Yang et al. (2015) also noticed improvements of the transparency of available photosynthetic radiation (T_{PAR}) and euphotic zone depth (Z_{eu}) for a lake in Japan by replacing the native QAA_{v5} with QAA_turbid. The current results indicate the underestimation of K_d, which is probably due to the IOP's retrieval, leading to the underestimation of Z_{SD}. The results also imply that the estimation of K_d and Z_{SD} can be improved when a new QAA approach is used, which was also confirmed by Yang et al. (2015), assuming that reparameterization of the semi-analytical scheme of Lee et al. (2015) is not required for oligo- to mesotrophic inland water. In addition, improvements can also be achieved by using different band combinations for the empirical steps of QAA (*e.g.*, red and NIR wavelengths) presented on other spatial platforms, such as Sentinel-2/3, and suggested for inland water dominated by inorganic or organic matter.

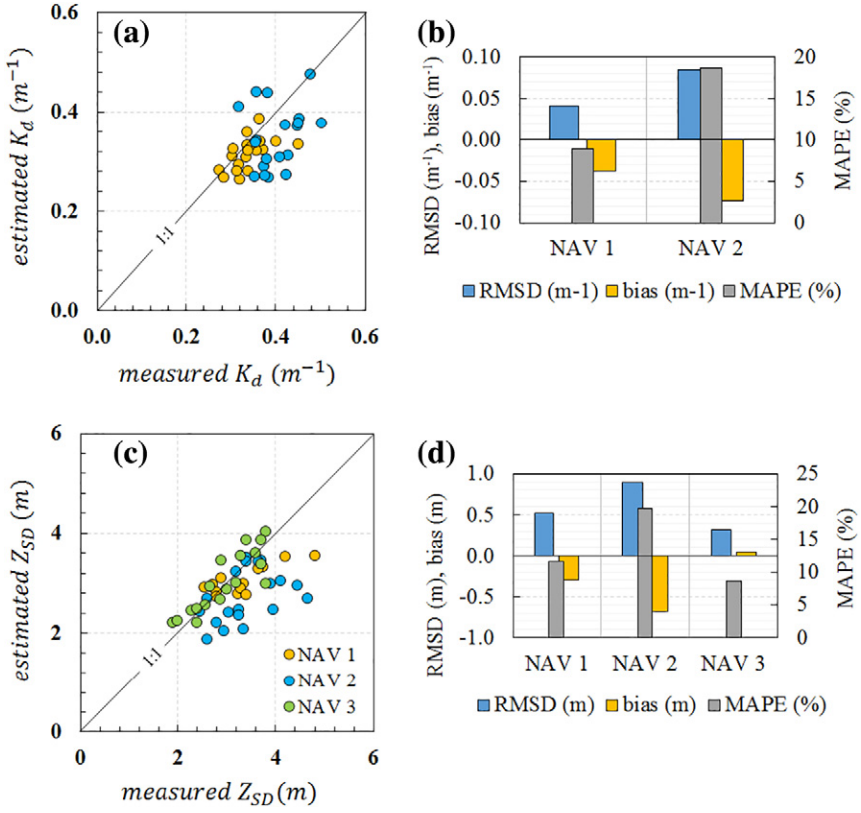

Fig. 6. (a) Relationship between estimated and measured K_d values using K_{dR17} and OLI bands, (b) Uncertainties of K_d represented by RMSD (m), bias (m), and MAPE (%). (c) Estimated and measured Z_{SD} values using Z_{SDR17} and OLI bands, (d) Uncertainties of Z_{SD}.

Furthermore, to compare the performance of the Z_{SD} model using three different QAA versions, a broader statistical analysis based on the Taylor and Target diagrams was applied. The terms magnitude and shape of two dataset patterns were considered, where the magnitude is related to the variance of the data retrieved by the model and the measured data, while the shape regards the agreement between modeled and measured data. The Taylor diagram allows us to discern how both magnitude and shape of the modeled data change as the model is modified (Jolliff et al., 2009).

Fig. 7 depicts the performances of all three approaches used in this work. With respect to Nav1 (Fig. 7a), both Z_{SDv5} ($\sigma^* = 0.78$, $R = 0.73$, and $uRMSD^* = 0.69$) and Z_{SDR17} ($\sigma^* = 0.44$, $R = 0.81$, and $uRMSD^* = 0.69$) show a good correlation with the measured data, which means that the distribution of the samples followed a similar pattern, matching the *in situ* Z_{SD} well.

The $uRMSD^*$ defines the distance of the modeled to the reference data. If the goal is to minimize the $uRMSD^*$, then the best situation is to have $\sigma^* = R$; however, this does not mean that the magnitude of the data dispersion will be low. It only means that the $uRMSD^*$ between the modeled and measured data is low, as depicted in Fig. 7a. The Z_{SD} retrieved using Z_{SDM14} ($\sigma^* = 0.91$, $R = 0.39$, and $uRMSD^* = 1.06$) presented the highest $uRMSD^*$ and the worst agreement with the reference data; however, σ^* almost reached the value 1, indicating that the magnitude of the data dispersion resembled the reference data. Based on the Target diagram (Fig. 7), all models underestimated the measured Z_{SD} in case of Nav1 (Fig. 7d). Models inside the circle indicate that the total RMSD is smaller than the standard deviation of the reference; this means, it is more desirable to obtain model values close to the reference. The distance between the reference and model is defined by the $RMSD^*$; therefore, the closest model was Z_{SDR17} ($RMSD^* = 0.83$ and $B^* = -0.45$), followed by Z_{SDv5} ($RMSD^* = 0.88$ and $B^* = -0.55$) and Z_{SDM14} ($RMSD^* = 1.13$ and $B^* = -0.40$). All of the models presented a negative bias and depicted a smaller standard deviation than that of the reference (Fig. 8a).

With respect to Nav2, Fig. 7b shows that the performances of both Z_{SDv5} ($\sigma^* = 1.00$, $R = 0.46$, and $uRMSD = 1.04$) and Z_{SDR17} ($\sigma^* = 0.86$, $R = 0.44$ and $uRMSD^* = 0.99$) are similar, which was expected because the improved version preserved the original framework of Z_{SDv5}. In addition, the correlation of both models was moderate, which means that the shape of the modeled and reference data does not match well (Fig. 8b). The model Z_{SDM14} ($\sigma^* = 2.54$, $R = 0.30$, and $uRMSD^* = 2.44$) exceeded the reference values; its position in the Taylor diagram was therefore far from that of the other models and reference. Fig. 7e shows that Z_{SDR17} had the lowest B^* ($RMSD^* = 1.49$ and $B^* = -1.11$) when compared with the reference; the standard deviation of Z_{SDv5} ($RMSD^* = 1.93$ and $B^* = -1.62$) was larger than that of the reference, while the standard deviation of Z_{SDR17} was lower than that of the reference. The Z_{SDM14} model ($RMSD^* = 2.50$ and $B^* = -0.57$) presented the worst performance, showing high errors compared with the reference.

Fig. 7c shows that Z_{SDR17} ($\sigma^* = 0.97$, $R = 0.86$, and $uRMSD^* = 0.51$) outperformed the results of other models (Z_{SDv5}: $\sigma^* = 1.10$, $R = 0.79$, and $uRMSD^* = 0.68$; Z_{SDM14}: $\sigma^* = 0.41$, $R = 0.88$, and $uRMSD^* = 0.67$), illustrating that the modification of QAA_{v5} improved the retrieval of Z_{SD}. In addition, the magnitude of the data dispersion of the reference and improved version were comparable and the correlation of both measures was good (Fig. 8c). The Target diagram highlights the advantage of Z_{SDR17} ($RMSD^* = 0.52$ and $B^* = 0.08$) over the other models (Z_{SDv5}: $RMSD^* = 1.59$ and $B^* = -1.44$; Z_{SDM14}: $RMSD^* = 2.02$ and $B^* = -1.91$). As previously mentioned, the use of QAA_{v5} led to an underestimation of Z_{SD}, justifying the use of the improved version.

3.4. Atmospheric correction assessment

To evaluate the semi-analytical model using orbital data and taking into account the availability of OLI/Landsat-8 images after two and three days of sample collection, three widely used atmospheric correction methods were tested and one atmospherically corrected product was evaluated. Aiming to compare both satellite (dimensionless) and TriOS data (sr^{-1}), the surface reflectance of OLI/Landsat-8 imagery, assumed to be the *in situ* data, was divided by π (Moses et al., 2012; Wang et al., 2015).

Fig. 9a shows that, of all the methods, L8SR performed well at station 13, collected with three-day delay of the OLI/Landsat-8 overpass. The coastal, blue, green, and red bands present a relative percentage error

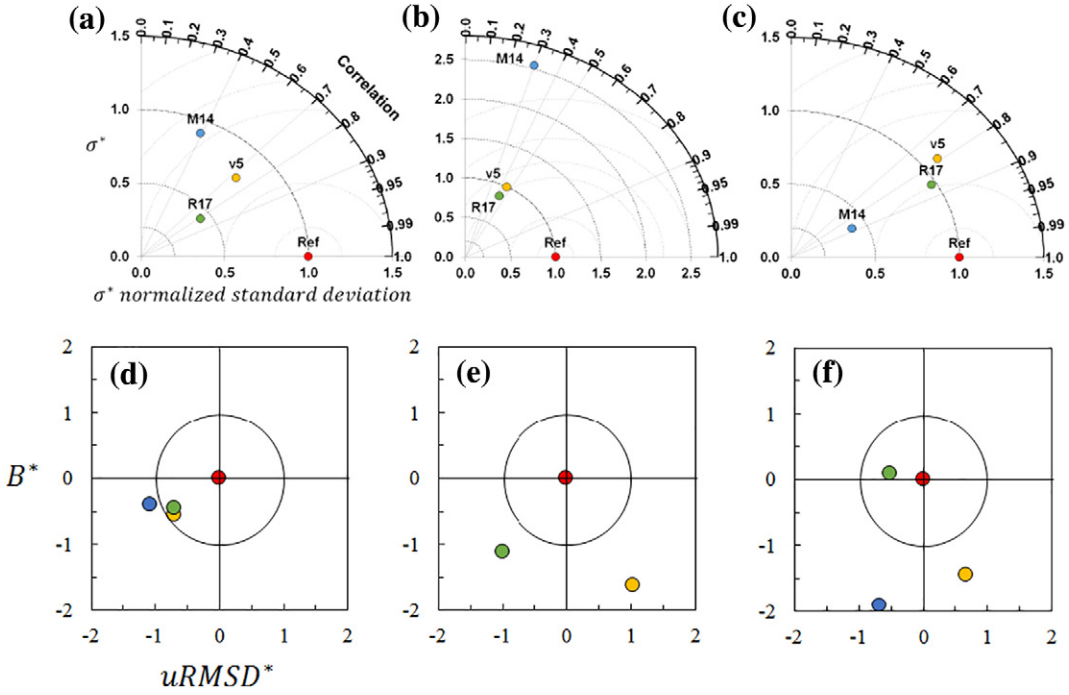

Fig. 7. Summary diagrams depicting the performances of the three models (Z_{SDv5}, Z_{SDM14} and Z_{SDR17}) in retrieving the Z_{SD} values. The Taylor diagram of (a) Nav1, (b) Nav2 and (c) Nav3 and the Target diagram of (d) Nav1, (e) Nav2 and (f) Nav3. The red dot refers to the reference data and the black circle corresponds to a $RMSD^*$ of 1.0.

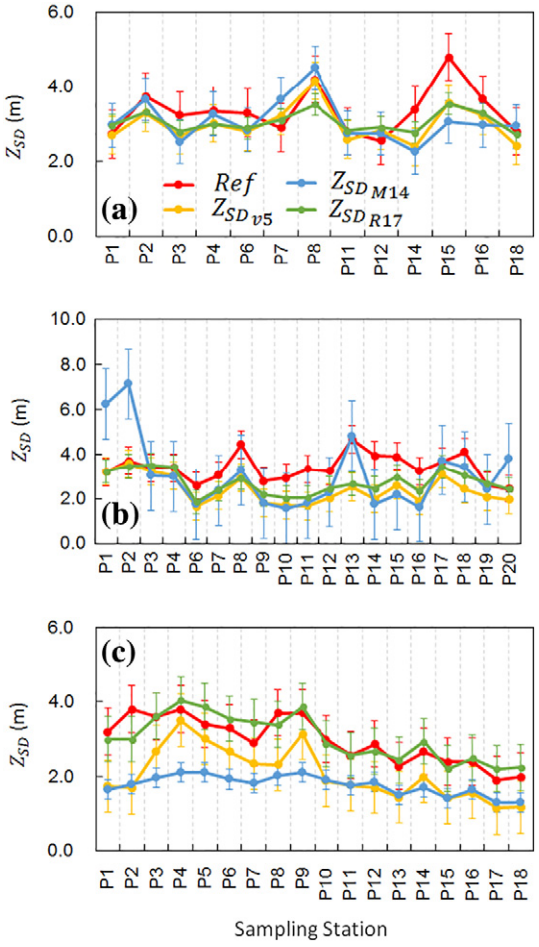

Fig. 8. Graphics depicting the Z_{SD} for each sampling station showing the values observed in the field (red line) and generated by different QAA versions (Z_{SDv5} – yellow line, Z_{SDM14} – blue line, Z_{SDR17} – green line) and based on different field campaigns: (a) Nav1, (b) Nav2 and (c) Nav3. The colored bars represent the standard deviation of each model and the reference data.

(ε) of 46.04%, 36.09%, 19.82%, and 46.40%, respectively; on the other hand, the NIR band shows the worst performance, with ε = 91.68%.

The second best result was acquired with ACOLITE for the coastal (391.72%), blue (34.69%), green (15.00%), red (32.16%), and NIR (110.27%) bands. The ε values of FLAASH were: coastal = 22.16%, blue = 141.44%, green = 51.77%, red = 113.82%, and NIR = 156.28%. The ε values of ATCOR were high, similar to FLAASH: blue (64.91%), green (82.13%), red (170.84%), and NIR (211.49%). The settings of both atmospheric corrections required similar information such as visibility and atmospheric and aerosol models. Regarding the retrieval of the IOPs in QAA, the presence of bands at 443, 482, 561, and 658 nm is mandatory; therefore, even with a good approximation of ACOLITE for the latter three bands, the worst result for the band at 443 nm of OLI/Landsat-8 prevents its use.

Based on Fig. 9b that shows the performance of the atmospheric correction considering station 17 with two-day delay of the OLI overpass, ACOLITE performed with a high accuracy mainly with respect to the blue (1.80%), red (2.47%), and NIR (9.85%) bands. In contrast, the coastal (630.12%) and green (34.13%) bands show the highest errors. The use of FLAASH reduced the error of the coastal band (9.68%) but not that of the blue (80.76%), green (30.25%), red (65.98%), and NIR (58.03%) bands. The L8SR provided more consistent results for all bands, even with the highest error for the coastal band (81.17%), followed by the blue (44.39%), green (19.23%), red (40.22%), and NIR (21.56%) bands. The ATCOR approach presented the following errors: coastal (44.94%), blue (64.11%), green (47.42%), red (103.32%), and NIR (58.03%).

The results clearly show the difficulty in correcting the bands at shorter wavelengths, such as coastal and blue bands, due to high scattering in those spectral regions. Several studies described this issue such as Kutser et al. (2016). Overall, L8SR achieved the best result; it was used in studies of the water quality in inland water, showing good outcomes in terms of spatial modeling of water quality parameters (Concha and Schott, 2016). Therefore, this product was selected to spatially display the Z_{SD} values.

3.5. Validation and long-term trend of Z_{SD}

The samples from the first campaign ($n = 6$) were separated from the whole dataset to validate the image data. The modified semi-analytical model () based on the L8SR product (Fig. 10) produced uncertainties in the two-day delay data ($n = 3$), with MAPE = 9.76%, RMSD = 0.31 m, and bias = −0.27 m, and in the three-day delay data ($n = 3$), with MAPE = 18.86%, RMSD = 0.79 m, and bias = −0.68 m. The bias observed in the data can be attributed to the date difference between *in situ* collection and satellite overpass.

Shang et al. (2016) applied the same approach to the Z_{SD} retrieval using MODIS images of the Bohai Sea, China. After validation ($n = 20$), they determined a RMSD of 0.126 m (log scale) and an average unbiased percentage difference (ε) of 23%. Applying the same error metrics as reported in Shang et al. (2016), our validation result ($n = 6$) presented a RMSD of 0.09 m and ε of 16%. These results show the potential of using OLI/Landsat-8 to monitor the water quality in this type of environment using orbital data with a temporal resolution of 16 days.

The Z_{SD} values for Nav were then derived using the QAA_{R17} version and the semi-analytical algorithm from Lee et al. (2015) and were further applied to OLI/Landsat-8 images corresponding to long periods in 2014 and 2016. The maps (Fig. 11) showed a distinct spatial and temporal variability. The lowest averages in 2014 were observed in January (1.69 ± 0.15 m) and December (1.74 ± 0.24 m), coherent with the wet season, where the system receives high loads of sediment *via* runoff, leading to the increase of the water turbidity. On the other hand, the months of August (3.03 ± 0.42 m) and April (2.99 ± 0.44 m) showed the highest averages, which is in agreement with the dry

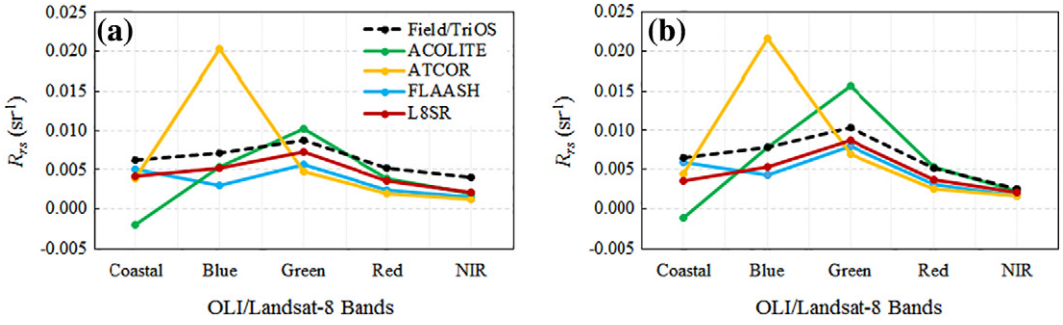

Fig. 9. Atmospheric correction method comparison for (a) station 13 (three-day delay) and (b) station 17 (two-day delay).

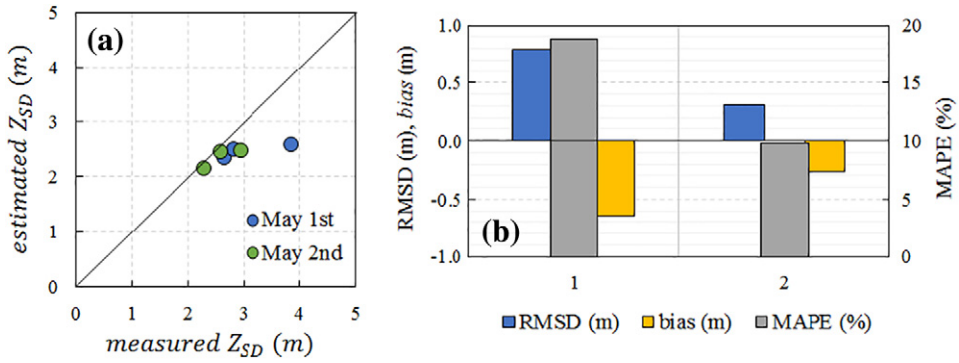

Fig. 10. Comparison between estimated Z_{SDR17} and *in situ* Z_{SD} (a) and error analysis (b). The estimated data were retrieved from the OLI/Landsat-8 image from May 4, 2014, while the *in situ* data refer to samples collected with a three-day (May 1, 2014) and two-day (May 2, 2014) temporal gap.

seasons. The zones A and B marked by the red circle (Fig. 11a) depict the regions with low Z_{SD}. The first one is placed in an area with many residential clusters, while zone B is mostly surrounded by sugar cane plantations. The wind and river dynamics also indicate the decrease of the Z_{SD} in zone B.

In general, the lowest Z_{SD} followed the wind direction; here, it is situated at the left border of the reservoir. The lowest averages of the Z_{SD} in 2016 occurred in February (1.40 ± 0.28 m) and January (1.44 ± 0.21 m), but the autumn months (March: 1.70 ± 0.23; April: 1.71 ± 0.24 m) also depicted low averages. On the contrary, the winter months showed the highest averages (June: 2.73 ± 0.26 m; July: 2.96 ± 0.24 m; and August: 2.90 ± 0.31 m). Such a seasonal variability was also reported by Wu et al. (2015) who observed the decrease of the transparency in spring and summer and an increase in winter. The reasons were attributed to the seasonal rainfall variation, which showed lower values in winter and higher values in spring and summer. In addition, the low transparency was also linked to the increase of phytoplankton biomass, indicating an exponential trend (LaBounty, 2008). The turbidity can be intensified by activities, such as sand dredging, which create sediment resuspension, leading to the decrease of the water clarity. In case of Nav, zone A is characterized by such activities.

The amount of rainfall (mm) in each season varied between 2014 and 2016 (Fig. 12). The rainfall in summer was significantly higher in 2016 (602.64 mm) than in 2014 (436.96 mm), while the difference in autumn (2014: 334.39 mm; 2016: 356.97 mm) and winter (2014: 127.58 mm; 2016: 130.05 mm) was insignificant. On the other hand, a distinct difference between both years was observed in spring (2014: 416.94 mm; 2016: 219.27 mm). Based on the Z_{SD} pattern for both years, an indirect relationship with the rainfall data can be observed, which was also reported in Wu et al. (2015).

Erosion due to rainfall and runoff intensifies the increase of suspended particles in inflowing streams, leading to the decrease of

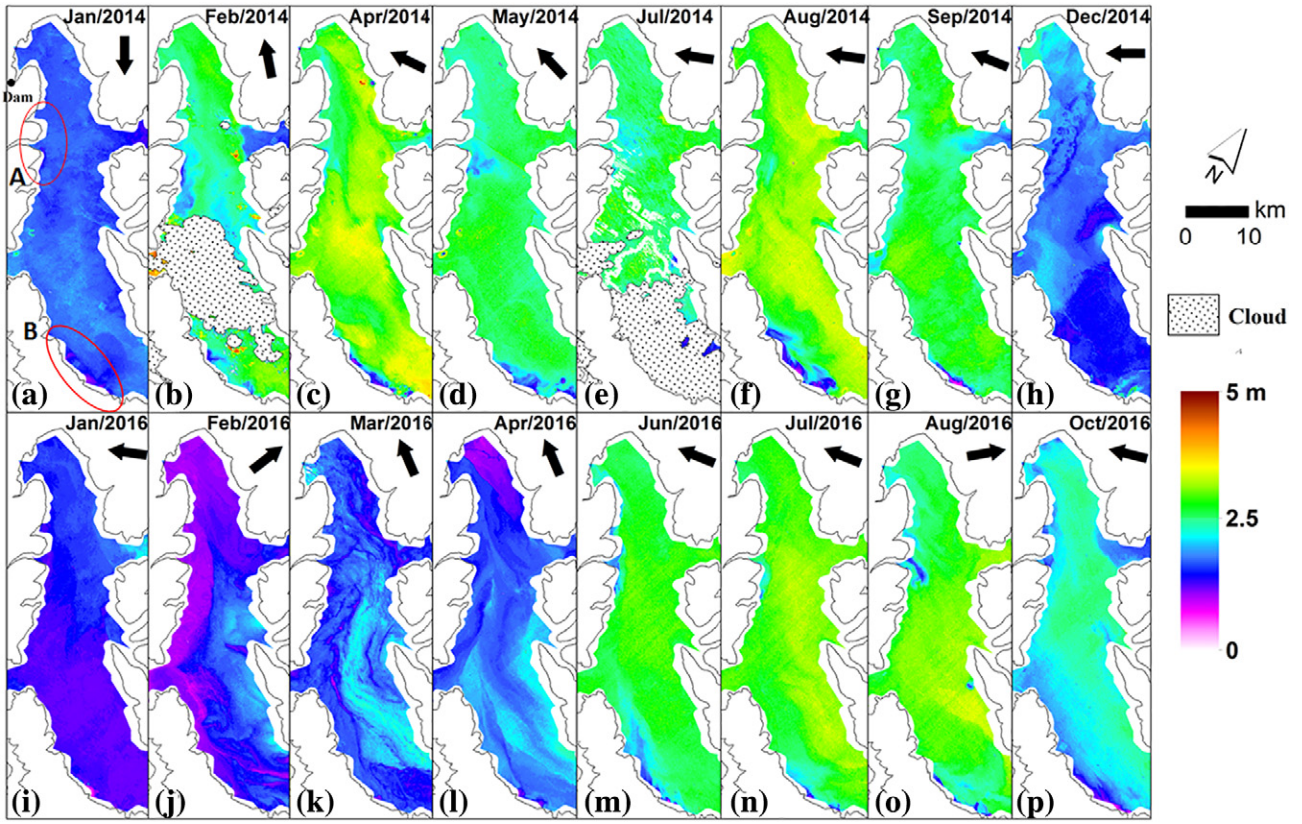

Fig. 11. Application of the semi-analytical model (Z_{SDR17}) to OLI/Landsat-8 images in different months of 2014 (a–h) and 2016 (i–p). The arrays represent the wind direction.

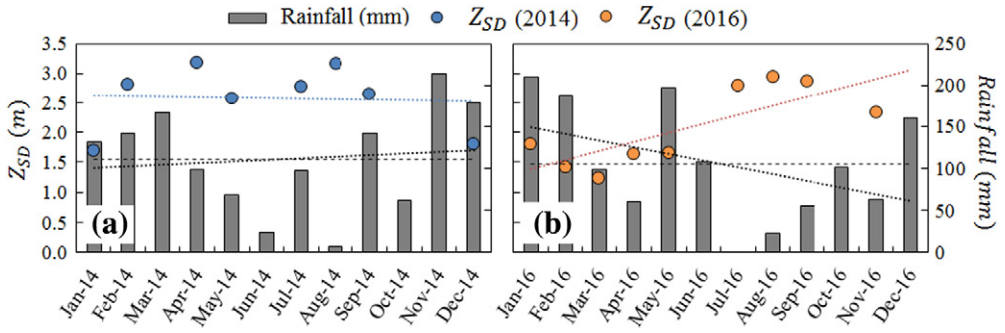

Fig. 12. Relationship between monthly rainfall (mm) and Z_{SD} in (a) 2014 and (b) 2016. The dashed black line marks the average rainfall, while the dotted black lines indicate the linear rainfall trend. The blue and orange dotted lines represent the linear Z_{SD} trends for 2014 and 2016, respectively.

the water transparency. This was expected and well documented. The wet season in 2016 is considered normal, with high values in January that decrease toward March. During this period, the Z_{SD} presented very low values, probably due to the input of sediment loads from the surrounding regions. On the contrary, the dry season led to an increase of the Z_{SD} values. The same pattern was also observed in 2014 but at different magnitudes.

4. Discussion

4.1. Relationships between Z_{SD} and water quality constituents

The water transparency is mostly represented by the Z_{SD} values and is a valuable parameter to study the water quality of all aquatic systems. The reason for the low or high water clarity can be attributed to watershed activities. With respect to the low Tietê River Basin, which includes Nav, the main use is agriculture with sugar cane plantations, citric cultures, and cattle raising. All these activities provide sediment load and nutrient (N and P) input to the water (Li et al., 2008). The enrichment of the water with nutrients promotes the increase of the primary production (Chl-*a* is a proxy), which highly correlates with $a_{\phi}(443)$. The inorganic and organic composition also affect the relationship between SPM and $a_{NAP}(443)$ (Le et al., 2015).

The relationship between the SPM and Chl-*a* concentrations was very weak (not shown here) when data from Nav1 and Nav2 were analyzed ($R = 0.37$). However, the relationship between those parameters was strong for Nav3 ($R = 0.80$), indicating different water compositions between field campaigns. These results indicate that 37% of the SPM dynamics can be explained by the Chl-*a* variations of Nav1 and Nav2, while 80% of the SPM variance can be explained by the Chl-*a* variations of Nav3. In addition, the correlation between SPM and tripton for Nav1 and Nav2 was strong ($R = 0.95$), while the correlation was 0.66 for Nav3. Based on these relationships, the SPM concentration of Nav1 and Nav2 was dominated by inorganic matter instead of organic matter due to the strong relationship between SPM and tripton; the contrary is true for Nav3 based on the weakest correlation.

Fig. 13 shows that the Z_{SD} is negatively correlated with SPM ($R = -0.6$, $p < 0.001$), turbidity, and Chl-*a* ($R = -0.5$ and $R = -0.4$, $p < 0.05$, respectively), which means that the water clarity deteriorates with increasing contribution of these parameters. In addition, the correlation between Z_{SD} and SPM is higher than that between Z_{SD} and Chl-*a*, suggesting that the water transparency is more affected by SPM than by Chl-*a*. The $a_{\phi}(443)$ highly correlates with the Chl-*a* concentration ($R = 0.7$, $p < 0.001$) and $a_{NAP}(443)$ with SPM ($R = 0.7$, $p < 0.001$). The source and nature of the SPM can be explained with the land use and land cover (LULC) analysis. Niyogi et al. (2006) observed a negative effect on grassland catchments that were converted to pasture. The main effect on

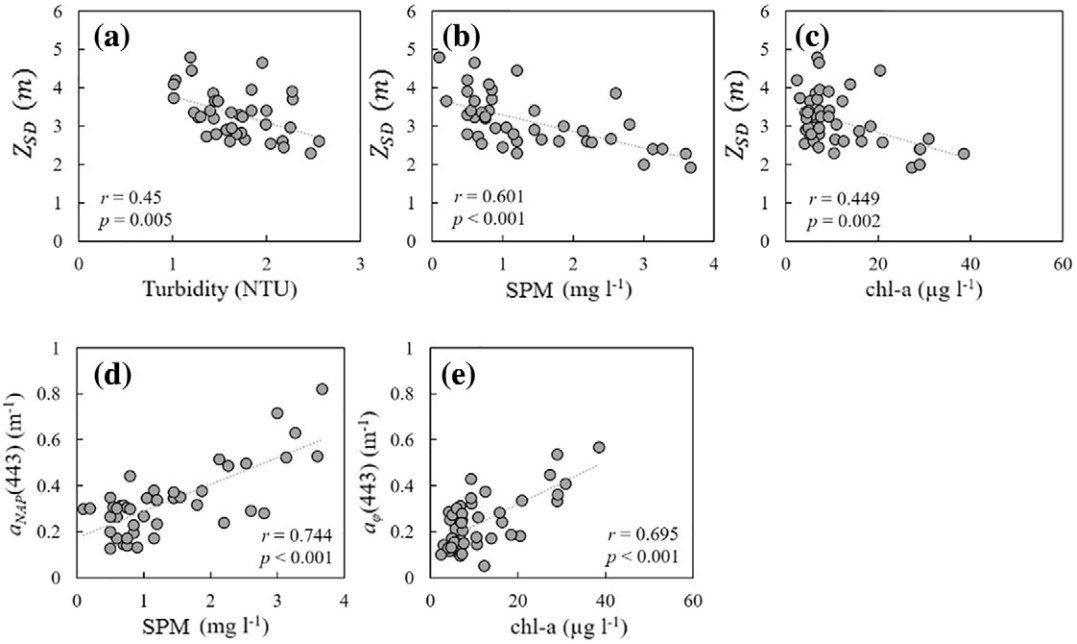

Fig. 13. Relationships between *in situ* Z_{SD} and *in situ* (a) turbidity, (b) SPM, and (c) Chl-*a* based on three field trips carried out in Nav.

physicochemical stream properties is often linked to increased nutrient concentrations and fine-sediment input. Increasing the sediment cover of the streambed would yield a linear decline of the water health. Agriculture reduces the water quality by increasing the nonpoint input of contaminants (Allan, 2004).

4.2. Limitations of model M1 in retrieving Z_{SD}

The estimation of IOPs using QAA_{v5} is the limiting factor for the success of Z_{SD} modeling, represented by step M1 (Fig. 2). Using the original QAA_{v5}, the values of Z_{SD} were underestimated (Fig. 5c), probably due to the underestimation of IOPs that led to the low performance of K_d (Fig. 5a). Li et al. (2016) also noticed the underestimation trend in the IOP retrieval using QAA_{v5} for turbid water and suggested that the larger contribution of particulate absorption at 440 nm leads to the poorer performance of the model. Similar results were observed for Nav dataset, where the contribution of a_{NAP} occupies most of the absorption budget (see Fig. 3), leading to the poor accuracy of QAA_{v5}. Ogashawara et al. (2016) highlighted that the calculation of $u(\lambda)$ (step 1 in Table 1) based on fixing the g_0 and g_1 values can lead to an underestimation of $a(\lambda)$. Both g_0 and g_1 are empirically derived and have direct influence on the magnitude of the irradiance reflectance to IOPs. The adjustment of these values can improve the estimation of a and b_b; however, additional tuning of the operational procedures is not recommended (Aurin and Dierssen, 2012).

Since the QAA uses R_{rs} as key parameter, it is worth noting that the *in situ* data collected to calculate R_{rs} is subjected to the random motion of the water surface and technique limitations. An accurate determination therefore remains a challenge (Lee et al., 2010). Although we used a robust method to reduce the sun glint to accurately determine R_{rs}, residual glint might remain; also, we need to consider the inherent noise produced by the sensors (Zibordi et al., 2012). Therefore, we also need to take the errors of the R_{rs} determination in consideration, which certainly will be propagated to the models M2 and M3.

Despite of the reparameterization of M1, the results are still not ideal and require further investigation. Based on the Taylor and Target diagrams, the shape and magnitude of the deviations of Z_{SD} are comparable to that of the reference. In other words, the Z_{SDv5} followed a pattern (high correlation) of data dispersion close to that of the reference and the variance of the data derived by the model resembled the variance of the reference (Fig. 8). However, these observations were not verified with Z_{SDM14}, highlighting the restriction of its use considering the water quality of Nav.

The uncertainty analysis carried out by Lee et al. (2010) showed that the contribution of $\Delta\eta$ over $\Delta a(\lambda)$ was more representative than that of $\Delta a(\lambda_0)$; this result was more related to water with low absorption but high scattering coefficients. For $a(\lambda)$ retrieval, η was slightly modified; however, due to the limitation of bands from OLI/Landsat-8, the band combination was maintained. Mishra et al. (2014) also used the same band combination from QAA_{v5} for turbid inland water. Lee et al. (2010) highlighted that, with the increase of $a(440)$, the uncertainties also increased to a certain extent. The success of $a(\lambda)$ derived by QAA also depends on b_{bp}; large uncertainties are related to high values of b_{bp}. Taking these outcomes into consideration, simple modifications of the empirical steps 2 and 4 (Table 1) were carried out and the model brought the derived Z_{SD} close to the 1:1 line, which was not possible with data from Nav2.

A close analysis of the bio-optical properties of Nav2 showed their higher variability, here represented by the coefficient of variation. The R_{rs}, for example, varied in magnitude and showed the highest coefficient of variance at the wavelengths of 443 and 560 nm (61% and 51%, respectively), which is probably due to particulate backscattering in the water, mainly at 560 nm (Lubac and Loisel, 2007). In addition, the high variability was also observed for the Chl-*a* concentration (CV = 46.76%) and the absorption coefficients of NAP (CV = 33.62%) and CDOM (CV = 17.31%) at 443 nm. The horizontal gradient observed in the bio-optical properties of Nav2 is the main constraint for Z_{SD} modeling when compared to datasets from all field trips. Thus, for waterbodies with a horizontal variability in bio-optical properties, the QAAs are limited to accurately model the IOPs and the estimation of Z_{SD} can therefore be compromised.

5. Conclusion

A semi-analytical scheme developed to estimate Z_{SD} was applied to Nav datasets using simulated OLI/Landsat-8 bands from three field trips carried out in 2014 and 2016. For validation, the OLI image-based Z_{SD} was compared with the *in situ* Z_{SD}; after improvements, a good relationship was observed, strongly suggesting the use of OLI/Landsat-8 data to map the water clarity in an oligo- to mesotrophic reservoir.

The algorithm inputs, such as the IOPs, K_d, and Z_{SD}, were semi-analytically derived, here denominated as steps M1, M2, and M3, respectively. The original quasi-analytical algorithm, QAA_{v5}, using bands from OLI was evaluated and further compared with QAA_{M14} using simulated bands from MSI, designed for turbid inland water. Both algorithms were used to derive K_d and Z_{SD}; however, the approach using QAA_{v5} outperformed QAA_{M14}, presenting a MAPE ranging between 10.35% and 19.76% for K_d and between 12.86% and 31.17% for Z_{SD}, while the latter model has a MAPE ranging between 12.68% to 28.29% for K_d and between 14.33% and 39.13% for Z_{SD}. Due to the underestimation of QAA_{v5} with respect to K_d and Z_{SD}, slight modifications (here named QAA_{R17}) of the empirical steps χ and η were carried out; thereafter, the estimated values moved close to the 1:1 line. The Taylor and Target diagrams showed that QAA_{R17} could retrieve Z_{SD} with high correlation and low uncertainty; however, this is not true for bio-optical properties with high variability. Of all the three datasets, Nav2 showed the highest coefficient of variance for remote sensing reflectance, suggesting a different biogeochemical composition along the reservoir.

To determine the best performance of QAA_{R17}, bio-optical characterization was carried out; Nav showed to be affected by NAP absorption in the visible spectral region. When the *in situ* Z_{SD} was compared with water quality parameters, SPM was negatively correlated, suggesting that the attenuation of light is generally dictated by suspended sediment. The need of an improved version of QAA_{v5} (step M1) for estimation highlighted the constraint of the model. However, this does not mean that the semi-analytical scheme from Lee et al. (2015) needs to be reparameterized; instead the current study recommends the use of a broader dataset covering different types of inland water to evaluate different QAA approaches and reach an universal format. Although, eventual modifications could be necessary based on the sensor configuration. Thus, the hypothesis that QAA_{v5} cannot accurately retrieve IOPs for inland water was confirmed, which means that step M1 is the limiting factor for Z_{SD} retrieval. However, the results also show that the mechanistic model proposed by Lee et al. (2015) can be considered as universally applicable.

Acknowledgements

The authors thank FAPESP Projects (Process N° 2012/19821-1 and 2015/21586-9) and Coordination for the Improvement of Higher Education Personnel (CAPES) for scholarship. The authors also thank Professor Edivaldo D. Velini and staffs from FCA/UNESP for allowing the use of their laboratory facilities and Dr. Shungudzemwoyo P. Garaba from University of Oldenburg for valuable discussion about remote sensing reflectance correction.

References

Aas, E., Høkedal, J., Sørensen, K., 2014. Secchi depth in the Oslofjord–Skagerrak area: theory, experiments and relationships to other quantities. Ocean Sci. 10:177–199. http://dx.doi.org/10.5194/os-10-177-2014.

Al Kaabi, M., Zhao, J., Ghedira, H., 2016. MODIS-based mapping of Secchi disk depth using a qualitative algorithm in the shallow Arabian Gulf. Remote Sens. 8 (423):1–17. http://dx.doi.org/10.3390/rs8050423.
Allan, J., 2004. Landscapes and riverscapes: the influence of land use on stream ecosystems. Annu. Rev. Ecol. Evol. Syst. 35:257–284. http://dx.doi.org/10.1146/annurev.ecolsys.35.120202.110122.
APHA/AWWA/WEF, 1998. Standard Methods for the Examination of Water and Wastewater. Washington, DC.
Aurin, D.A., Dierssen, H.M., 2012. Advantages and limitations of ocean color remote sensing in CDOM-dominated: mineral-rich coastal and estuarine waters. Remote Sens. Environ. 125, 181–197.
Barsi, J., Lee, K., Kvaran, G., Markham, B., Pedelty, J., 2014. The spectral response of the Landsat-8 operational land imager. Remote Sens. 6:10232–10251. http://dx.doi.org/10.3390/rs61010232.
Buiteveld, H., 1995. A model for calculation of diffuse light attenuation (PAR) and Secchi depth. Neth. J. Aquat. Ecol. 29:55–65. http://dx.doi.org/10.1007/bf02061789.
Cavenaghi, A.L., Velini, E.D., Galo, M.L.B.T., Carvalho, F.T., Negrisoli, E., Trindade, M.L.B., Simionato, J.L.A., 2003. Caracterização da qualidade de água e sedimento relacionados com a ocorrência de plantas aquáticas em cinco reservatórios da bacia do rio Tietê. Planta Daninha 21, 43–52.
Cheng, C., Wei, Y., Sun, X., Zhou, Y., 2013. Estimation of chlorophyll-a concentration in turbid Lake using spectral smoothing and derivative analysis. Int. J. Environ. Res. Public Health 10:2979–2994. http://dx.doi.org/10.3390/ijerph10072979.
Coelho, C., Cardoso, D., Firpo, M., 2015. Precipitation diagnostics of an exceptionally dry event in São Paulo, Brazil. Theor. Appl. Climatol. 125:769–784. http://dx.doi.org/10.1007/s00704-015-1540-9.
Comitê da Bacia Hidrográfica do Baixo Tietê (CBH-BT), 2009. Fundamentos para a implantação da cobrança pelo uso dos recursos hídricos [WWW Document]. http://www.sigrh.sp.gov.br/public/uploads/documents/7406/fundamentacao_cobranca_bt.pdf (accessed 1. 3. 16).
Concha, J., Schott, J., 2016. Retrieval of color producing agents in case 2 waters using Landsat 8. Remote Sens. Environ. 185:95–107. http://dx.doi.org/10.1016/j.rse.2016.03.018.
Curtarelli, M., Ogashawara, I., Alcântara, E., Stech, J., 2015. Coupling remote sensing bio-optical and three-dimensional hydrodynamic modeling to study the phytoplankton dynamics in a tropical hydroelectric reservoir. Remote Sens. Environ. 157:185–198. http://dx.doi.org/10.1016/j.rse.2014.06.013.
Dekker, A.G., 1993. Detection of optical water quality parameters for eutrophic waters by high resolution remote sensing. PhD. thesis, Vrije Universiteit, Amsterdam, p. 222.
Doron, M., Babin, M., Mangin, A., Hembise, O., 2007. Estimation of light penetration, and horizontal and vertical visibility in oceanic and coastal waters from surface reflectance. J. Geophys. Res. 112:1–15. http://dx.doi.org/10.1029/2006jc004007.
European Space Agency, 2016. Sentinel-2 MSI Document Library - User Guides - Sentinel Online [WWW Document]. Sentinel.esa.int https://sentinel.esa.int/web/sentinel/user-guides/sentinel-2-msi/document-library/ (accessed 2. 3. 16).
Franz, B., Bailey, S., Kuring, N., Werdell, P., 2015. Ocean color measurements with the operational land Imager on Landsat-8: implementation and evaluation in SeaDAS. J. Appl. Remote. Sens. 9, 096070. http://dx.doi.org/10.1117/1.jrs.9.096070.
Friedrichs, M.A., Carr, M.E., Barber, R.T., Scardi, M., Antoine, D., Armstrong, R.A., ... Christian, J.R., 2009. Assessing the uncertainties of model estimates of primary productivity in the tropical Pacific Ocean. J. Mar. Syst. 76 (1):113–133. http://dx.doi.org/10.1016/j.jmarsys.2008.05.010.
Fukushima, T., Matsushita, B., Oyama, Y., Yoshimura, K., Yang, W., Terrel, M., Kawamura, S., Takegahara, A., 2015. Semi-analytical prediction of Secchi depth using remote-sensing reflectance for lakes with a wide range of turbidity. Hydrobiologia 780: 5–20. http://dx.doi.org/10.1007/s10750-015-2584-7.
Garaba, S.P., Voß, D., Wollschläger, J., Zielinski, O., 2015. Modern approaches to shipborne ocean color remote sensing. Appl. Opt. 54 (12):3602–3612. http://dx.doi.org/10.1364/AO.54.003602.
Gitelson, A., 1992. The peak near 700 nm on radiance spectra of algae and water: relationships of its magnitude and position with chlorophyll concentration. Int. J. Remote Sens. 13:3367–3373. http://dx.doi.org/10.1080/01431169208904125.
Golterman, H.L., Clymo, R.S., Ohnstad, M.A.M., 1978. Methods for Physical and Chemical Analysis of Freshwater. Blackwell Scientific Publications, Oxford (213 pp.).
Gordon, H., 1995. Remote sensing of ocean color: a methodology for dealing with broad spectral bands and significant out-of-band response. Appl. Opt. 34:8363–8374. http://dx.doi.org/10.1364/ao.34.008363.
Gordon, H., Brown, O., Jacobs, M., 1975. Computed relationships between the inherent and apparent optical properties of a flat Homogeneous Ocean. Appl. Opt. 14: 417–427. http://dx.doi.org/10.1364/ao.14.000417.
Gücker, B., Silva, R.C., Graeber, D., Monteiro, J.A., Boëchat, I.G., 2016. Urbanization and agriculture increase exports and differentially alter elemental stoichiometry of dissolved organic matter (DOM) from tropical catchments. Sci. Total Environ. 550: 785–792. http://dx.doi.org/10.1016/j.scitotenv.2016.01.158.
Jolliff, J.K., Kindle, J.C., Shulman, I., Penta, B., Friedrichs, M.A., Helber, R., Arnone, R.A., 2009. Summary diagrams for coupled hydrodynamic-ecosystem model skill assessment. J. Mar. Syst. 76 (1):64–82. http://dx.doi.org/10.1016/j.jmarsys.2008.05.014.
Kirk, J., 1975. A theoretical analysis of the contribution of algal cells to the attenuation of light within natural waters I. General treatment of suspensions of pigmented cells. New Phytol. 75:11–20. http://dx.doi.org/10.1111/j.1469-8137.1975.tb01366.x.
Kong, J., Sun, X., Wong, D., Chen, Y., Yang, J., Yan, Y., Wang, L., 2015. A semi-analytical model for remote sensing retrieval of suspended sediment concentration in the Gulf of Bohai, China. Remote Sens. 7:5373–5397. http://dx.doi.org/10.3390/rs70505373.
Kutser, T., Paavel, B., Verpoorter, C., Ligi, M., Soomets, T., Toming, K., Casal, G., 2016. Remote sensing of Black Lakes and using 810 nm reflectance peak for retrieving water quality parameters of optically complex waters. Remote Sens. 8:497. http://dx.doi.org/10.3390/rs8060497.
LaBounty, J.F., 2008. Secchi transparency of Boulder Basin, Lake Mead, Arizona-Nevada: 1990–2007. Lake Reservoir Manage. 24 (3):207–218. http://dx.doi.org/10.1080/07438140809354062.
Le, C., Li, Y., Zha, Y., Sun, D., Yin, B., 2009. Validation of a quasi-analytical algorithm for highly turbid eutrophic water of Meiliang Bay in Taihu Lake, China. IEEE Trans. Geosci. Remote Sens. 47:2492–2500. http://dx.doi.org/10.1109/tgrs.2009.2015658.
Le, C., Lehrter, J., Hu, C., Schaeffer, B., MacIntyre, H., Hagy, J., Beddick, D., 2015. Relation between inherent optical properties and land use and land cover across Gulf Coast estuaries. Limnol. Oceanogr. 60:920–933. http://dx.doi.org/10.1002/lno.10065.
Lee, Z., Carder, K., Arnone, R., 2002. Deriving inherent optical properties from water color: a multiband quasi-analytical algorithm for optically deep waters. Appl. Opt. 41: 5755–5772. http://dx.doi.org/10.1364/ao.41.005755.
Lee, Z., Darecki, M., Carder, K.L., Davis, C.O., Stramski, D., Rhea, W.J., 2005a. Diffuse attenuation coefficient of downwelling irradiance: an evaluation of remote sensing methods. J. Geophys. Res. 110:1–9. http://dx.doi.org/10.1029/2004jc002573.
Lee, Z.P., Du, K.P., Arnone, R., 2005b. A model for the diffuse attenuation coefficient of downwelling irradiance. J. Geophys. Res. Oceans 110 (C2). http://dx.doi.org/10.1029/2004JC002275.
Lee, Z., Lubac, B., Werdell, J., Arnone, R., 2009. An Update of the Quasi-Analytical Algorithm (QAA_v5) [WWW Document]. http://www.ioccg.org/groups/Software_OCA/QAA_v5.pdf (accessed 11. 3. 14).
Lee, Z., Ahn, Y.H., Mobley, C., Arnone, R., 2010. Removal of surface-reflected light for the measurement of remote-sensing reflectance from an above-surface platform. Opt. Express 18 (25):26313–26324. http://dx.doi.org/10.1364/OE.18.026313.
Lee, Z., Hu, C., Shang, S., Du, K., Lewis, M., Arnone, R., Brewin, R., 2013. Penetration of UV-visible solar radiation in the global oceans: insights from ocean color remote sensing. J. Geophys. Res. Oceans 118:4241–4255. http://dx.doi.org/10.1002/jgrc.20308.
Lee, Z., Shang, S., Hu, C., Du, K., Weidemann, A., Hou, W., Lin, J., Lin, G., 2015. Secchi disk depth: a new theory and mechanistic model for underwater visibility. Remote Sens. Environ. 169:139–149. http://dx.doi.org/10.1016/j.rse.2015.08.002.
Lee, Z., Shang, S., Qi, L., Yan, J., Lin, G., 2016. A semi-analytical scheme to estimate Secchi-disk depth from Landsat-8 measurements. Remote Sens. Environ. 177:101–106. http://dx.doi.org/10.1016/j.rse.2016.02.033.
Li, S., Gu, S., Liu, W., Han, H., Zhang, Q., 2008. Water quality in relation to land use and land cover in the upper Han River basin, China. Catena 75:216–222. http://dx.doi.org/10.1016/j.catena.2008.06.005.
Li, S., Song, K., Mu, G., Zhao, Y., Ma, J., Ren, J., 2016. Evaluation of the quasi-analytical algorithm (QAA) for estimating total absorption coefficient of turbid inland waters in Northeast China. IEEE Journal of Selected Topics in Applied Earth Observations and Remote Sensing 9:4022–4036. http://dx.doi.org/10.1109/jstars.2016.2549026.
Lubac, B., Loisel, H., 2007. Variability and classification of remote sensing reflectance spectra in the eastern English Channel and southern North Sea. Remote Sens. Environ. 110 (1):45–58. http://dx.doi.org/10.1016/j.rse.2007.02.012.
Majozi, N., Salama, M., Bernard, S., Harper, D., Habte, M., 2014. Remote sensing of euphotic depth in shallow tropical inland waters of Lake Naivasha using MERIS data. Remote Sens. Environ. 148:178–189. http://dx.doi.org/10.1016/j.rse.2014.03.025.
Mishra, D.R., Narumalani, S., Rundquist, D., Lawson, M., 2005. Characterizing the vertical diffuse attenuation coefficient for downwelling irradiance in coastal waters: implications for water penetration by high resolution satellite data. ISPRS J. Photogramm. Remote Sens. 60 (1):48–64. http://dx.doi.org/10.1016/j.isprsjprs.2005.09.003.
Mishra, S., Mishra, D., Lee, Z., 2014. Bio-optical inversion in highly turbid and cyanobacteria-dominated waters. IEEE Trans. Geosci. Remote Sens. 52:375–388. http://dx.doi.org/10.1109/tgrs.2013.2240462.
Mobley, C.D., 1994. Light and Water: Radiative Transfer in Natural Waters. Academic Press, San Diego.
Mobley, C.D., 1995. Hydrolight 3.0 User's Guide. SRI International, California.
Mobley, C.D., 1999. Estimation of the remote-sensing reflectance from above-surface measurements. Appl. Opt. 38 (36), 7442–7455.
Morel, A., 1988. Optical modeling of the upper ocean in relation to its biogenous matter content (case I waters). J. Geophys. Res. 93:10749–10768. http://dx.doi.org/10.1029/jc093ic09p10749.
Morel, A., Maritorena, S., 2001. Bio-optical properties of oceanic waters: a reappraisal. J. Geophys. Res. Oceans 106:7163–7180. http://dx.doi.org/10.1029/2000jc000319.
Moses, W., Gitelson, A., Perk, R., Gurlin, D., Rundquist, D., Leavitt, B., Barrow, T., Brakhage, P., 2012. Estimation of chlorophyll-a concentration in turbid productive waters using airborne hyperspectral data. Water Res. 46:993–1004. http://dx.doi.org/10.1016/j.watres.2011.11.068.
Mueller, J.L., 2000a. SeaWiFS algorithm for the diffuse attenuation coefficient, K(490), using water-leaving radiances at 490 and 555 nm. In: Hooker, S.B. (Ed.), Sea-WiFS Postlaunch Calibration and Validation Analyses, Part 3. NASA Goddard Space Flight Cent, Greenbelt, Md, pp. 24–27.
Mueller, J.L., 2000b. In-water radiometric profile measurements and data analysis protocols. In: Fargion, G.S., Mueller, J.L. (Eds.), Ocean Optics Protocols for Satellite Ocean Color Sensor Validation. NASA Tech. Memo, Goddard Space Flight Center, Greenbelt, Maryland, pp. 87–97 (2000209966/Rev2 1).
Niyogi, D., Koren, M., Arbuckle, C., Townsend, C., 2006. Stream communities along a catchment land-use gradient: subsidy-stress responses to pastoral development. Environ. Manag. 39:213–225. http://dx.doi.org/10.1007/s00267-005-0310-3.
Ogashawara, I., Mishra, D.R., Nascimento, R.F.F., Alcântara, E.H., Kampel, M., Stech, J.L., 2016. Re-parameterization of a quasi-analytical algorithm for colored dissolved organic matter dominant inland waters. Int. J. Appl. Earth Obs. Geoinf. 53:128–145. http://dx.doi.org/10.1016/j.jag.2016.09.001 (ISSN 0303–2434).
Pahlevan, N., Schott, J.R., Franz, B.A., Zibordi, G., Markham, B., Bailey, S., Schaaf, C.B., Ondrusek, M., Greb, S., Strait, C.M., 2017. Landsat 8 remote sensing reflectance

(Rrs) products: evaluations, intercomparisons, and enhancements. Remote Sens. Environ. 190, 289–301 https://doi.org/10.1016/j.rse.2016.12.030 (ISSN 0034–4257).
Petesse, M., Petrere Jr., M., Agostinho, Â., 2014. Defining a fish bio-assessment tool to monitoring the biological condition of a cascade reservoirs system in tropical area. Ecol. Eng. 69:139–150. http://dx.doi.org/10.1016/j.ecoleng.2014.03.070.
Preisendorfer, R., 1986. Secchi disk science: visual optics of natural waters. Limnol. Oceanogr. 31:909–926. http://dx.doi.org/10.4319/lo.1986.31.5.0909.
Riddick, C., Hunter, P., Tyler, A., Martinez-Vicente, V., Horváth, H., Kovács, A., Vörös, L., Preston, T., Présing, M., 2015. Spatial variability of absorption coefficients over a biogeochemical gradient in a large and optically complex shallow lake. J. Geophys. Res. Oceans 120:7040–7066. http://dx.doi.org/10.1002/2015jc011202.
Rodgher, S., Espíndola, E., Rocha, O., Fracácio, R., Pereira, R., Rodrigues, M., 2005. Limnological and ecotoxicological studies in the cascade of reservoirs in the Tietê River (São Paulo, Brazil). Braz. J. Biol. 65:697–710. http://dx.doi.org/10.1590/s1519-69842005000400017.
Rodrigues, T., Guimarães, U., Rotta, L., Watanabe, F., Alcântara, E., Imai, N., 2016. Delineamento amostral em reservatórios utilizando imagens Landsat-8/OLI: um estudo de caso no reservatório de Nova Avanhandava (Estado De São Paulo, Brasil). Boletim de Ciências Geodésicas 22:303–323. http://dx.doi.org/10.1590/s1982-21702016000200017.
Rotta, L., Mishra, D., Alcântara, E., Imai, N., 2016. Analyzing the status of submerged aquatic vegetation using novel optical parameters. Int. J. Remote Sens. 37:3786–3810. http://dx.doi.org/10.1080/01431161.2016.1204027.
Shang, S., Lee, Z., Shi, L., Lin, G., Wei, G., Li, X., 2016. Changes in water clarity of the Bohai Sea: observations from MODIS. Remote Sens. Environ. 186:22–31. http://dx.doi.org/10.1016/j.rse.2016.08.020.
Simis, S., Peters, S., Gons, H., 2005. Remote sensing of the cyanobacterial pigment phycocyanin in turbid inland water. Limnol. Oceanogr. 50:237–245. http://dx.doi.org/10.4319/lo.2005.50.1.0237.
Smith, R., Baker, K., 1981. Optical properties of the clearest natural waters (200–800 nm). Appl. Opt. 20:177–184. http://dx.doi.org/10.1364/ao.20.000177.
Smith, W., Espíndola, E., Rocha, O., 2014. Environmental gradient in reservoirs of the medium and low Tietê River: limnological differences through the habitat sequence. Acta Limnologica Brasiliensia 26:73–88. http://dx.doi.org/10.1590/s2179-975x2014000100009.
Tassan, S., Ferrari, G., 1995. An alternative approach to absorption measurements of aquatic particles retained on filters. Limnol. Oceanogr. 40:1358–1368. http://dx.doi.org/10.4319/lo.1995.40.8.1358.
Tassan, S., Ferrari, G., 1998. Measurement of light absorption by aquatic particles retained on filters: determination of the optical pathlength amplification by the 'transmittance-reflectance' method. J. Plankton Res. 20:1699–1709. http://dx.doi.org/10.1093/plankt/20.9.1699.
Taylor, K.E., 2001. Summarizing multiple aspects of model performance in a single diagram. J. Geophys. Res. Atmos. 106 (D7):7183–7192. http://dx.doi.org/10.1029/2000JD900719.
Tilstone, G., Moore, G.F., Sorensen, K., Doerffer, R., Rottgers, R., Ruddick, K.G., Pasterkamp, R., Jorgensen, P.V., 2002. REVAMP, Regional Validation of MERIS Chlorophyll Products in North Sea Coastal Waters, Protocols. European Union FPV: EVG1 CT 2001 00049 (68 pp.).
Toole, D.A., Siegel, D.A., 2001. Modes and mechanisms of ocean color variability in the Santa Barbara Channel. J. Geophys. Res. Oceans 106 (C11):26985–27000. http://dx.doi.org/10.1029/2000JC000371.
Torloni, C.E.C., Corrêa, A.R.A., Carvalho Jr., A.A., Santos, J.J., Gonçalves, J.L., Gereto, E.J., Cruz, J.A., Moreira, J.A., Silva, D.C., Deus, E.F., Ferreira, A.S., 1993. Produção pesqueira e composição das capturas em reservatórios sob concessão da CESP nos rios Tietê, Paraná e Grande, no período de 1986 a 1991. Série Pesquisa e Desenvolvimento, São Paulo (73 pp.).
Tyler, J., 1968. The Secchi disc. Limnol. Oceanogr. 13:1–6. http://dx.doi.org/10.4319/lo.1968.13.1.0001.
United States Geological Survey, 2016. Landsat Surface Reflectance High Level Data Products [WWW Document]. Landsat.usgs.gov http://landsat.usgs.gov/CDR_LSR.php (accessed 8. 3. 16).
Vanhellemont, Q., Ruddick, K., 2014. Turbid wakes associated with offshore wind turbines observed with Landsat 8. Remote Sens. Environ. 145:105–115. http://dx.doi.org/10.1016/j.rse.2014.01.009.
Vanhellemont, Q., Ruddick, K., 2015. Advantages of high quality SWIR bands for ocean colour processing: examples from Landsat-8. Remote Sens. Environ. 161:89–106. http://dx.doi.org/10.1016/j.rse.2015.02.007.
Wang, H., Hladik, C., Huang, W., Milla, K., Edmiston, L., Harwell, M., Schalles, J., 2010. Detecting the spatial and temporal variability of chlorophyll- a concentration and total suspended solids in Apalachicola Bay, Florida using MODIS imagery. Int. J. Remote Sens. 31:439–453. http://dx.doi.org/10.1080/01431160902893485.
Wang, S., Li, J., Shen, Q., Zhang, B., Zhang, F., Lu, Z., 2015. MODIS-based radiometric color extraction and classification of inland water with the Forel-Ule scale: a case study of Lake Taihu. IEEE Journal of Selected Topics in Applied Earth Observations and Remote Sensing 8:907–918. http://dx.doi.org/10.1109/jstars.2014.2360564.
Watanabe, F., Mishra, D., Astuti, I., Rodrigues, T., Alcântara, E., Imai, N., Barbosa, C., 2016a. Parametrization and calibration of a quasi-analytical algorithm for tropical eutrophic waters. ISPRS J. Photogramm. Remote Sens. 121:28–47. http://dx.doi.org/10.1016/j.isprsjprs.2016.08.009.
Watanabe, F., Rodrigues, T., Bernardo, N., Alcântara, E., Imai, N., 2016b. Drought can cause phytoplankton growth intensification in Barra Bonita reservoir. Modeling Earth Systems and Environment 2:1–7. http://dx.doi.org/10.1007/s40808-016-0193-8.
Wu, Z., Zhang, Y., Zhou, Y., Liu, M., Shi, K., Yu, Z., 2015. Seasonal-spatial distribution and long-term variation of transparency in Xin'anjiang reservoir: implications for reservoir management. Int. J. Environ. Res. Public Health 12 (8):9492–9507. http://dx.doi.org/10.3390/ijerph120809492.
Yacobi, Y., Moses, W., Kaganovsky, S., Sulimani, B., Leavitt, B., Gitelson, A., 2011. NIR-red reflectance-based algorithms for chlorophyll-a estimation in mesotrophic inland and coastal waters: Lake Kinneret case study. Water Res. 45:2428–2436. http://dx.doi.org/10.1016/j.watres.2011.02.002.
Yan, Y., Sydor, M., 2006. Surface for remote sensing reflectance in case 2 waters of Lake superior. J. Great Lakes Res. 32:407–414. http://dx.doi.org/10.3394/0380-1330(2006)32[407:SCFRSR]2.0.CO;2.
Yang, W., Matsushita, B., Chen, J., Yoshimura, K., Fukushima, T., 2013. Retrieval of inherent optical properties for turbid inland waters from remote-sensing reflectance. IEEE Trans. Geosci. Remote Sens. 51:3761–3773. http://dx.doi.org/10.1109/tgrs.2012.2220147.
Yang, W., Matsushita, B., Chen, J., Yoshimura, K., Fukushima, T., 2014. Application of a semianalytical algorithm to remotely estimate diffuse attenuation coefficient in turbid inland waters. IEEE Geosci. Remote Sens. Lett. 11:1046–1050. http://dx.doi.org/10.1109/lgrs.2013.2284343.
Yang, W., Matsushita, B., Yoshimura, K., Chen, J., Fukushima, T., 2015. A modified semianalytical algorithm for remotely estimating euphotic zone depth in turbid inland waters. IEEE Journal of Selected Topics in Applied Earth Observations and Remote Sensing 8 (4):1545–1554. http://dx.doi.org/10.1109/JSTARS.2015.2415853.
Yunus, A., Dou, J., Sravanthi, N., 2015. Remote sensing of chlorophyll-a as a measure of red tide in Tokyo Bay using hotspot analysis. Remote Sens. Appl. Soc. Environ. 2:11–25. http://dx.doi.org/10.1016/j.rsase.2015.09.002.
Zaneveld, J., Pegau, W., 2003. Robust underwater visibility parameter. Opt. Express 11:2997. http://dx.doi.org/10.1364/oe.11.002997.
Zibordi, G., Ruddick, K., Ansko, I., Moore, G., Kratzer, S., Icely, J., Reinart, A., 2012. In situ determination of the remote sensing reflectance: an inter-comparison. Ocean Sci. 8:567–586. http://dx.doi.org/10.5194/os-8-567-2012.